NAVAL POSTGRADUATE SCHOOL

MONTEREY, CALIFORNIA

THESIS

RELATIONSHIPS BETWEEN ARCTIC ICE WATER FRACTION AND LOCAL 2D WIND STRESSES AT THE SURFACE OF THE CRYOSPHERE

by

Michael C. Becker II

December 2021

Thesis Advisor:	Timothy P. Stanton
Co-Advisor:	William J. Shaw
Second Reader:	Jaclyn L. Kinney

Approved for public release. Distribution is unlimited.

THIS PAGE INTENTIONALLY LEFT BLANK

REPORT DOCUMENTATION PAGE	*Form Approved OMB No. 0704-0188*

Public reporting burden for this collection of information is estimated to average 1 hour per response, including the time for reviewing instruction, searching existing data sources, gathering and maintaining the data needed, and completing and reviewing the collection of information. Send comments regarding this burden estimate or any other aspect of this collection of information, including suggestions for reducing this burden, to Washington headquarters Services, Directorate for Information Operations and Reports, 1215 Jefferson Davis Highway, Suite 1204, Arlington, VA 22202-4302, and to the Office of Management and Budget, Paperwork Reduction Project (0704-0188) Washington, DC 20503.

1. AGENCY USE ONLY *(Leave blank)*	2. REPORT DATE December 2021	3. REPORT TYPE AND DATES COVERED Master's thesis

4. TITLE AND SUBTITLE
RELATIONSHIPS BETWEEN ARCTIC ICE WATER FRACTION AND LOCAL 2D WIND STRESSES AT THE SURFACE OF THE CRYOSPHERE

5. FUNDING NUMBERS

6. AUTHOR(S) Michael C. Becker II

7. PERFORMING ORGANIZATION NAME(S) AND ADDRESS(ES)
Naval Postgraduate School
Monterey, CA 93943-5000

8. PERFORMING ORGANIZATION REPORT NUMBER

9. SPONSORING / MONITORING AGENCY NAME(S) AND ADDRESS(ES)
N/A

10. SPONSORING / MONITORING AGENCY REPORT NUMBER

11. SUPPLEMENTARY NOTES The views expressed in this thesis are those of the author and do not reflect the official policy or position of the Department of Defense or the U.S. Government.

12a. DISTRIBUTION / AVAILABILITY STATEMENT
Approved for public release. Distribution is unlimited.

12b. DISTRIBUTION CODE
A

13. ABSTRACT (maximum 200 words)

A study of the Marginal Ice Zone (MIZ) in the Central Arctic was sponsored by the Office of Naval Research (ONR) in 2014. This experiment used clusters of buoys equipped with autonomous sensors. As the 2014 arctic season progressed, the buoy GPS locations were collected to produce estimates of local divergence of the ice field, and a resulting measurement of equivalent Open Water Fraction (eOWF). In this research, changes in eOWF within the MIZ were compared with local two-dimensional 10 m wind fields extracted from the local European Centre for Medium-Range Weather Forecasts (ECMWF) reanalysis wind products. A cross-correlation analysis between the mean field surface stresses (wind stress, divergence, and curl) and eOWF ice divergence was conducted along the buoy GPS tracks using a Lagrangian sampling method. OWF from the NASA Team Special Sensor Microwave/Imager (SSMI) satellite measurements algorithm was compared with the eOWF ice divergence calculation method. Results revealed that wind stress goes through a relaxation period of about one day prior to large eOWF changes. For convergent events starting with high eOWF, changes are seen < 24 hours after a relaxation period. A strong cross correlation between eOWF and wind stress was confirmed with mean r-values of 0.91 and 0.89 across two clusters of buoy data. Timelag between the maximum wind stress and the point of lowest wind stress when eOWF rate of change is highest is about 60 hours.

14. SUBJECT TERMS
Arctic, Marginal Ice Zone, Canada Basin, Beaufort Sea, Open Water Fraction, lead, divergence, convergence, curl, bulk stress, wind stress, European Centre for Medium-Range Weather Forecasts, ECMWF, NASA team Special Sensor Microwave/Imager, SSM/I, cross correlation, relaxation period, ice divergence, eOWF, Lagrangian

15. NUMBER OF PAGES
87

16. PRICE CODE

17. SECURITY CLASSIFICATION OF REPORT	18. SECURITY CLASSIFICATION OF THIS PAGE	19. SECURITY CLASSIFICATION OF ABSTRACT	20. LIMITATION OF ABSTRACT
Unclassified	Unclassified	Unclassified	UU

NSN 7540-01-280-5500

Standard Form 298 (Rev. 2-89)
Prescribed by ANSI Std. 239-18

THIS PAGE INTENTIONALLY LEFT BLANK

Approved for public release. Distribution is unlimited.

RELATIONSHIPS BETWEEN ARCTIC ICE WATER FRACTION AND LOCAL 2D WIND STRESSES AT THE SURFACE OF THE CRYOSPHERE

Michael C. Becker
Lieutenant Commander, United States Navy
BSAST, Thomas A Edison State College, 2005
MS, Florida International University, 2008

Submitted in partial fulfillment of the
requirements for the degree of

**MASTER OF SCIENCE IN METEOROLOGY
AND PHYSICAL OCEANOGRAPHY**

from the

**NAVAL POSTGRADUATE SCHOOL
December 2021**

Approved by: Timothy P. Stanton
Advisor

William J. Shaw
Co-Advisor

Jaclyn L. Kinney
Second Reader

Peter C. Chu
Chair, Department of Oceanography

THIS PAGE INTENTIONALLY LEFT BLANK

ABSTRACT

A study of the Marginal Ice Zone (MIZ) in the Central Arctic was sponsored by the Office of Naval Research (ONR) in 2014. This experiment used clusters of buoys equipped with autonomous sensors. As the 2014 arctic season progressed, the buoy GPS locations were collected to produce estimates of local divergence of the ice field, and a resulting measurement of equivalent Open Water Fraction (eOWF). In this research, changes in eOWF within the MIZ were compared with local two-dimensional 10 m wind fields extracted from the local European Centre for Medium-Range Weather Forecasts (ECMWF) reanalysis wind products. A cross-correlation analysis between the mean field surface stresses (wind stress, divergence, and curl) and eOWF ice divergence was conducted along the buoy GPS tracks using a Lagrangian sampling method. OWF from the NASA Team Special Sensor Microwave/Imager (SSMI) satellite measurements algorithm was compared with the eOWF ice divergence calculation method. Results revealed that wind stress goes through a relaxation period of about one day prior to large eOWF changes. For convergent events starting with high eOWF, changes are seen < 24 hours after a relaxation period. A strong cross correlation between eOWF and wind stress was confirmed with mean r-values of 0.91 and 0.89 across two clusters of buoy data. Timelag between the maximum wind stress and the point of lowest wind stress when eOWF rate of change is highest is about 60 hours.

THIS PAGE INTENTIONALLY LEFT BLANK

TABLE OF CONTENTS

I. BACKGROUND 1
- A. NAVAL APPLICATIONS 1
- B. DECLINING TREND OF ARCTIC SEA ICE 3
- C. BEAUFORT SEA 6
- D. MARGINAL ICE ZONE 8
- E. ICE-ALBEDO FEEDBACK 11

II. THESIS: RELATIONSHIPS BETWEEN ARCTIC ICE WATER FRACTION AND LOCAL 2D WIND STRESSES AT THE SURFACE OF THE CRYOSPHERE 15
- A. INTRODUCTION OF COUPLING ATMOSPHERE TO OCEAN 15
- B. METHODS 19
  - 1. DATA SETS 19
  - 2. ECMWF WIND FIELD STRESS, DIVERGENCE, AND CURL 21
  - 3. MIZ BUOY CLUSTER eOWF 23
  - 4. SSMI OWF 27
  - 5. WIND DIRECTION 28
  - 6. ANALYSIS TOOLS 28
  - 7. TEMPORAL and SPATIAL CONSIDERATIONS 30
- C. RESULTS 35
- D. DISCUSSION 47
- E. CONCLUSION 58

SUPPLEMENTAL: ADDITIONAL MATLAB RESULTS 63

LIST OF REFERENCES 65

INITIAL DISTRIBUTION LIST 71

THIS PAGE INTENTIONALLY LEFT BLANK

LIST OF FIGURES

Figure 1. Russian military arctic infrastructure. Source: Boulègue (2019).....2

Figure 2. Arctic ice coverage. Source: USNIC (2021).....4

Figure 3. CMIP6 simulations Source: CMIP6 (2021).....5

Figure 4. Beaufort Gyre. Source: AMAP (1998). 6

Figure 5. Ice Age, 1984 to 2018. Source: NSIDC (2021a). 8

Figure 6. MIZ research project. Source: MIZ (2014).....9

Figure 7. Seasonal ice retreat and advance. Source: Lee (2017).....10

Figure 8. Observed annual mean and all sky planetary albedo for entire arctic. Source: Perovich (2005). 13

Figure 9. Mean seasonal cycle in sea ice albedo CERES vs. SHEBA mean. Source: Perovich (2005). 14

Figure 10. Ice drift rate to Geostrophic wind speed. Source: Hibler (1981).....16

Figure 11. Upwelling near the MIZ. Source: Hibler (1981). 17

Figure 12. Ocean forcing. Source: Mellor (1996).....18

Figure 13. Divergence. 22

Figure 14. Curl. 23

Figure 15. Buoy GPS Tracks.....24

Figure 16. Buoy area changes during seasonal drift. 25

Figure 17. Small angle filter.....26

Figure 18. Piecewise eOWF.....27

Figure 19. Inverse tangent and atan2 function. 28

Figure 20. Cross-correlation temporal test.....31

Figure 21. Spatial smoothing.....32

Figure 22. Spatial context.....33

Figure 23. Heat map example....34

Figure 24. Annual overview of Cluster 4....36

Figure 25. Wind Event overview, +/-6 day (+/-144-hour) Centered on YD 206, Cluster 4....37

Figure 26. Cross correlation of eOWF and Wind Stress, YD 206, Cluster 4....39

Figure 27. Wind Event overview, +/-6 day (+/-144-hour) Centered on YD 128, Cluster 4....40

Figure 28. Cross correlation of eOWF with Divergence, and Curl, YD 128, Cluster 4....41

Figure 29. Annual overview of Cluster 1....42

Figure 30. Wind Event overview, +/-6 day (+/-144-hour) Centered on YD 119, Cluster 1....43

Figure 31. Cross correlation of eOWF and Wind Stress, YD 119, Cluster 1....44

Figure 32. Data heat map, Cluster 4....46

Figure 33. Data heat map, Cluster 1....47

Figure 34. Relaxation period, Cluster 4....49

Figure 35. Relaxation period, Cluster 1....50

Figure 36. eOWF vs. SSMI OWF, Cluster 4....51

Figure 37. eOWF vs. SSMI OWF, Cluster 1....52

Figure 38. Cross correlation coefficient “r,” Cluster 4....53

Figure 39. Cross correlation coefficient “r,” Cluster 1....53

Figure 40. Normalized correlation coefficient (NCC), Cluster 4....54

Figure 41. Normalized correlation coefficient (NCC), Cluster 1....55

Figure 42. Cluster 4 and 1 response comparison....57

Figure 43. Cluster 4 and 1 track comparison, YD 205....58

Figure 44. SSMI OWF gradient....60

LIST OF ACRONYMS AND ABBREVIATIONS

2D	two-dimensional
BS	Beaufort Sea
CMIP	Coupled Model Intercomparison Project
DOD	Department of Defense
ECMWF	European Center for Medium-Range Weather Forecasts
eOWF	equivalent Open Water Fraction
GPS	Global Positioning System
IPCC	Intergovernmental Panel on Climate Change
MIZ	Marginal Ice Zone
NASA	National Aeronautics and Space Administration
NATO	North Atlantic Treaty Organization
ONR	Office of Naval Research
SHEBA	Surface Heat Budget of the Arctic Ocean
SSMI	Special Sensor Microwave/Imager
SSP	Shared Socioeconomic Pathways
TL	Time Lag
USNIC	U.S. National Ice Center

THIS PAGE INTENTIONALLY LEFT BLANK

ACKNOWLEDGMENTS

I would like to give special thanks to Professor Tim Stanton for his guidance through the research and writing process. The COVID-19 pandemic made in-person meetings and discussions impossible for the vast majority of my time at NPS. Professor Stanton's support during lockdown was very encouraging. Regardless of the barriers, we were able to persevere and accomplish a rigorous study of the Arctic Marginal Ice Zone. I was pleased to finish on schedule and provide relevant feedback for future numerical modeling. I am very grateful to have had such an exceptional thesis advisor.

My wife, Magda, always supported me through the many study hours and research stages. I hope the time we sacrificed for my education will provide us with a bright future that we will share together. Thank you for being a wonderful spouse and a wonderful mother to our children.

THIS PAGE INTENTIONALLY LEFT BLANK

I. BACKGROUND

A. NAVAL APPLICATIONS

The United States is an Arctic Nation (DOD 2019). The Department of Defense (DOD) has established a strategy for the Arctic region that addresses the current era of great power competition. The 2019 DOD Arctic Strategy falls within the guidance of the 2018 National Defense Strategy and has emphasized three specific end-states for the Arctic region. These end states are building Arctic awareness, enhancing Arctic operations, and strengthening the rules-based order in the Arctic. This thesis will provide scientific results that contribute to the Enhancing of Arctic Operations through the advancement of understating environmental dynamics within the Marginal Ice Zone (MIZ).

The Arctic is encompassed by eight nations (USN 2021). Seven are allies and partners, while one is not. The U.S. has strong defensive and scientific relationships with four North Atlantic Treaty Organization (NATO) allies in the Arctic: Canada, the Kingdom of Denmark (Greenland), Iceland and Norway. The prospect of armed conflict in the Arctic remains low; however, new trends in the physical state of the Arctic environment have opened opportunity to complex strategic competition. These changes include the increased availability of commercial shipping lanes, access to previously untapped natural resources, and the necessity to maintain order within a more active infrastructure. The lure of tourism has also become a growing factor as large populations begin to travel through the Arctic region during the summer season.

As a result of decreased seasonal ice coverage in the Arctic, there is more commercial investment, shorter trade routes, and expanded access to natural deposits. The U.S. is not the only government that is responding to the new Arctic environment. The Russian government has modernized its military bases in the Arctic and operations have increased significantly (Boulègue 2019). The layout of recent Russian military upgrades spans the most northern regions (Figure 1).

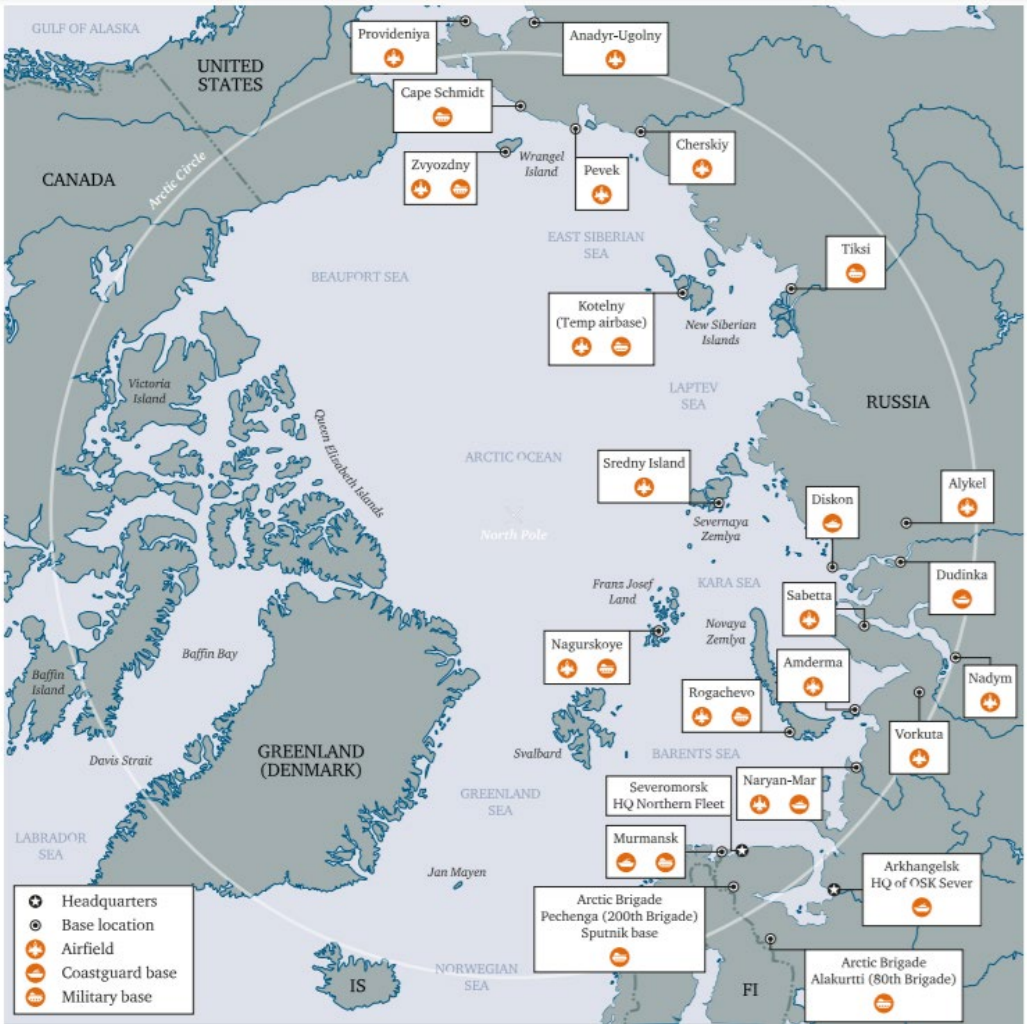

The Russian military has invested heavily into infrastructure stretching across the Arctic coast. The type of base is provided by the imbedded key on the map.

Figure 1. Russian military arctic infrastructure. Source: Boulègue (2019).

The DOD and Homeland Security have responded through each branch of service to ensure the protection of U.S. national security interests in the Arctic. In addition, China has attempted to gain influence in the Arctic through investment and governance using the Belt and Road Initiative as a pathway to new trade routes and resources (DOD 2019). China also has plans to build Arctic-class shipping, anticipating the widening window of navigable Arctic waters. The great power competition is alive and developing quickly in the Arctic.

In response to the physical and political changes in the Arctic, the U.S. Navy has been tasked to provide flexible deterrent options in the Arctic (DOD 2019). Commander, U.S. 2nd Fleet is dual hatted as Commander of NATO's Joint Force Command Norfolk. The 2nd Fleet will be ready to exercise, maintain and exploit Sea Control in the Arctic through interoperability with the U.S. Coast Guard. Of great interest, is the Navy's role in protecting sea lines of communication, humanitarian relief and rescue in the Arctic. To meet this developing mission, future investment in Arctic navigation will be necessary as the USN begins to operate more frequently north of the Arctic Circle.

The Navy's Arctic Blueprint "A Blue Arctic," issues a mandate for science and technology to add to the fight in the Arctic (USN 2021). This research answers that call by exploring new methods of determining the opening seasonal ice pack within the MIZ, supporting safe Naval operations in a shifting Arctic environment. The Navy will modernize future Arctic forces that will deploy manned and unmanned patrols in ice-diminished waters. The arrival of new operational platforms means more presence by the DOD. As Arctic operations mature over the next decades, the Navy's credibility will rise enabling effective enforcement of a rules-based region. This thesis is a direct contribution towards "Enhancing Arctic Operations and Building Arctic Awareness," (DOD 2019).

B. DECLINING TREND OF ARCTIC SEA ICE

Modeling sea ice in the Arctic is conducted through a collaboration between several U.S. government agencies. Investments come from the National Oceanic Atmospheric Administration, Department of Energy, National Aeronautics and Space Administration (NASA), National Science Foundation and the DOD. Within the DOD, the U.S. National Ice Center (USNIC) is an interagency organization that includes NOAA, USCG, and is led by the USN. The USNIC provides a range of Arctic environmental information to the U.S. government, including snow products and ice forecasting (Figure 2).

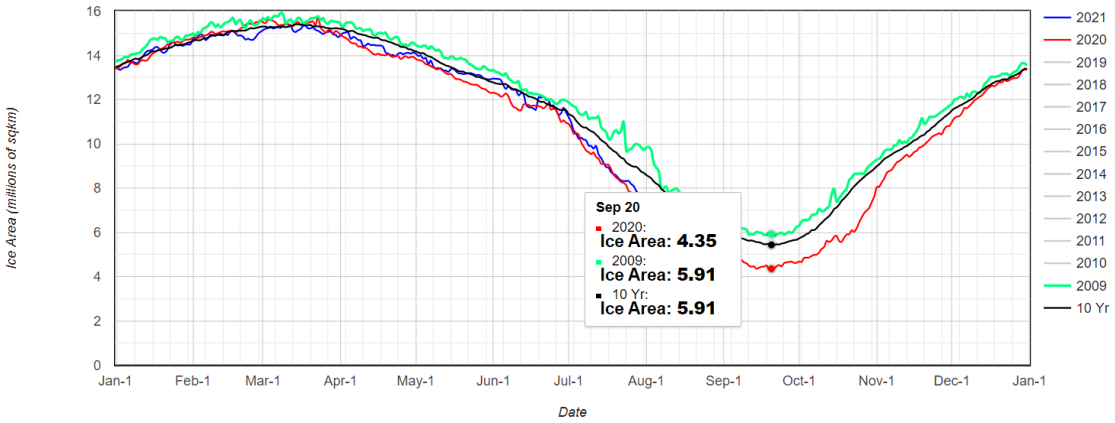

Ice area coverage is provided for 2020 in red, 10 year mean in black, and 2009 in green. The ice area minimum is marked on the plot for comparison.

Figure 2. Arctic ice coverage. Source: USNIC (2021).

For many years, it has been observed that the Arctic ice area is shrinking. Late summer ice extent has fallen by 1.56 million square kilometers during the last decade. In 2020 the Arctic ice minimum was 4.35 million square kilometers, compared to 5.91 million square kilometers observed in 2009 (USNIC 2021). Ice thickness also decreased significantly during this period of reduced late summer areal extent.

Observations show that Arctic sea ice area has been significantly decreasing for many decades. Some models predict that the Arctic summer will be ice free by 2050 (CMIP6), (Figure 3).

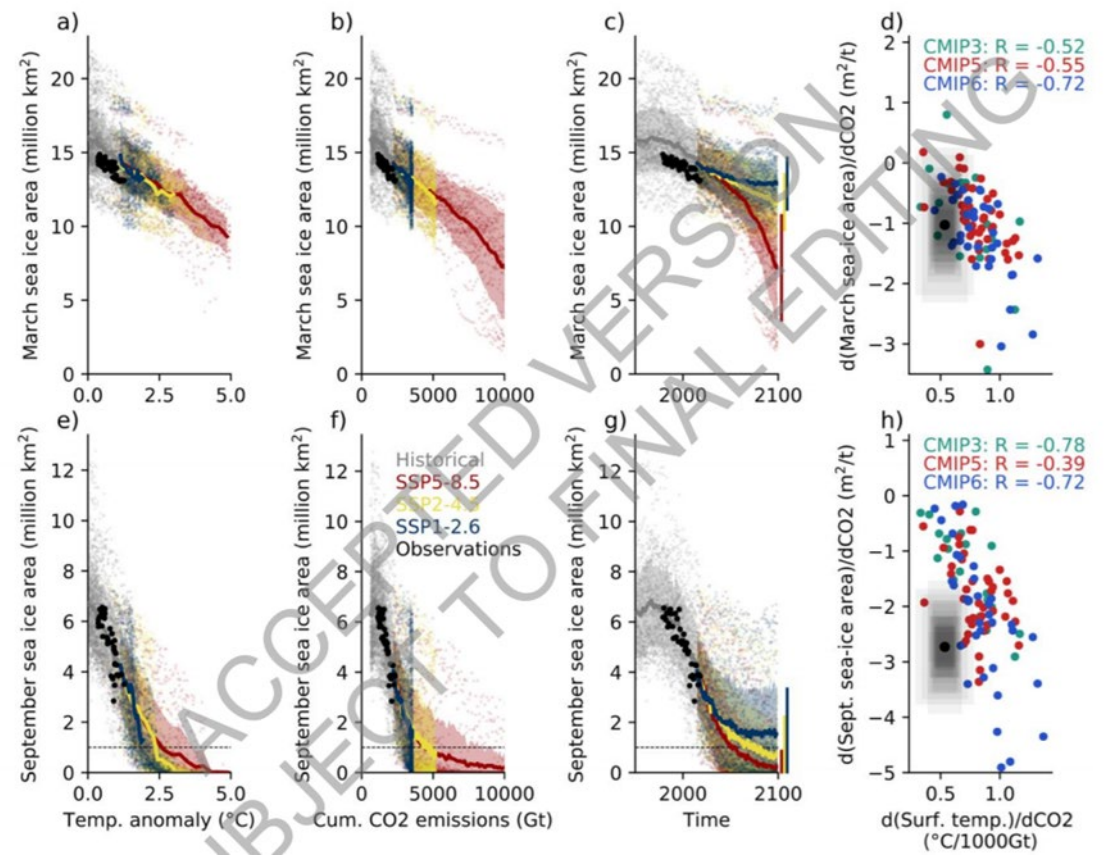

Monthly mean March (a-d) and September (e-h) sea-ice area as a function of global surface air temperature (GSAT) anomaly (a,e); cumulative anthropogenic CO_2 emissions (b,f); year (c,g) in CMIP6 model simulations (shading, ensemble mean as bold line) and in observations (black dots). Panels d and h show the sensitivity of sea-ice loss to anthropogenic CO_2 emissions as a function of the modelled sensitivity of GSAT to anthropogenic CO_2 emissions. In panels d and h, the black dot denotes the observed sensitivity, while the shading around it denotes internal variability as inferred from CMIP6 simulations (after Notz and SIMIP Community, 2020). Further details on data sources and processing are available in the chapter data table (Table 9.SM.9).

ACCEPTED VERSION SUBJECT TO FINAL EDITING

Figure 3. CMIP6 simulations Source: CMIP6 (2021).

The Intergovernmental Panel on Climate Change (IPCC) Coupled Model Intercomparison Project (CMIP) has formed ensembles of model predictions and observations, showing that model bias may cause underestimation of the actual rate of change in sea ice. Additionally, the future March ice maximum may retract to current September minimum extents by 2100 if present CO_2 emission trajectories continue, as shown by using Shared Socioeconomic Pathways (SSP) scenario 8.5 (AR6 2021). While there are many other environmental markers, the rapid decrease in Arctic sea ice area should be interpreted as an obvious indicator of ongoing climate change.

C. BEAUFORT SEA

The ice and atmospheric data collected for this thesis was measured by drifting ice-deployed buoys in the Beaufort Sea (BS). The BS is an area of the Arctic Ocean located north of Alaska and the Canada Yukon that is mostly covered by ice, except during the late summer season between August and September. A large wind driven anti-cyclonic (clockwise) gyre exists in the BS as a result of a semi-permanent atmospheric high-pressure system over the region (Petty 2016, figure 4). The BS contributes to the Transpolar Drift that pushes ice out of the Arctic into the Atlantic Ocean, largely through the Fram Strait, east of Greenland.

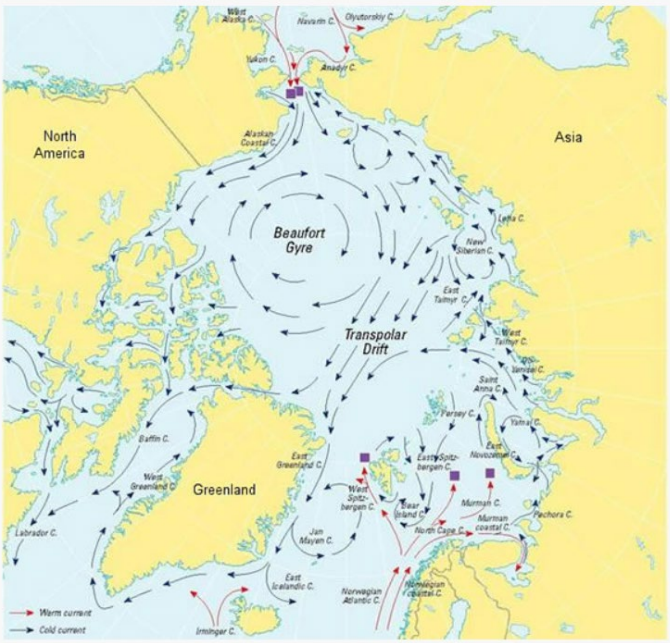

Arctic Ocean circulation.

—Image courtesy of Arctic Monitoring and Assessment Programme (AMAP), Figure 3.29, AMAP (1998).

Arrows represent prevailing surface currents in the Arctic.

Figure 4. Beaufort Gyre. Source: AMAP (1998).

An important contributor to the strength of the Beaufort Gyre is the Arctic Oscillation (AO). The AO is an alternating atmospheric pressure pattern between the mid-latitudes and the Arctic regions of the North Pacific and North Atlantic (Higgins 2002). If

the AO has a positive pressure dome over the Arctic, then storms shear northward due to a stronger mid-latitude (sub-tropical) jet stream. This has an effect of minimizing cold air outbreaks into the mid-latitudes and increasing the storms in the Arctic. When the AO has a negative pressure dome over the arctic, the polar jet dips farther south, steering Arctic air into the mid-latitudes (Polar vortex) and moderating the freezing temperatures in the Arctic. The AO is influenced by the strength of seasonal low-pressure areas near Iceland and the Aleutians Islands. The AO can shift the Beaufort Gyre center and its resulting ice floe, which can influence the Transpolar Drift strength (Proshutinsky 2019). The ice that forms in the Beaufort Gyre can circulate for several years before it melts or exits via the Transpolar Drift. Sea ice that stays within the Beaufort Gyre has more time to grow into multiyear ice resulting in a thick, ridged, and rafted ice pack (Shu et al. 2020). However, this long-lived ice is becoming rare because of the widespread increase in late summer melt seen in recent years. The Beaufort Gyre pushes a significant fraction of multiyear ice up against the Canada Archipelago (Figure 5), (World Atlas 2021). Multiyear ice builds up there and becomes the thickest ice in the Arctic. Recent years have shown a significant loss of multiyear ice buildup in the BS compared to past accumulations.

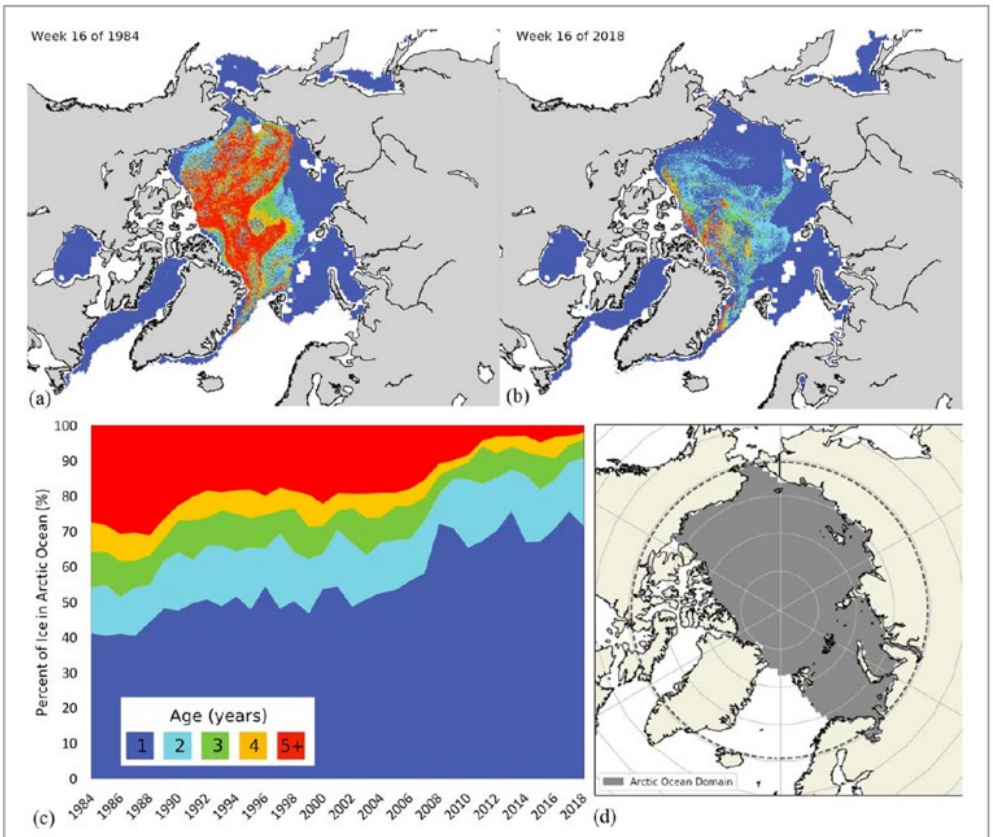

Figure 4. Ice age during week 16 (last week of April) in 1984(a) and 2018 (b) (adapted from the National Snow and Ice Data Center (NSIDC)), and time series of percent of total extent of different age classes (c) as averaged over the Arctic Ocean Domain (insert). Note the data for 2018 is preliminary data courtesy M Tschudi (University of Colorado).

Figure 5. Ice Age, 1984 to 2018. Source: NSIDC (2021a).

D. MARGINAL ICE ZONE

This study uses data from the multi-disciplinary, Office of Naval Research (ONR) sponsored Marginal Ice Zone (MIZ) research project, which included an extensive field program in the BS during the summer of 2014 (Figure 6). Traditionally a MIZ is defined as a part of the seasonal ice pack that varies in width (5 to 200 kilometers) that extends from the ice edge into the ice pack, where waves and swell strongly force ice breakup. This region is characterized by highly variable ice conditions and a broken-up ice pack. In general, it is wider in the Antarctic than the Arctic (NSIDC 2021b).

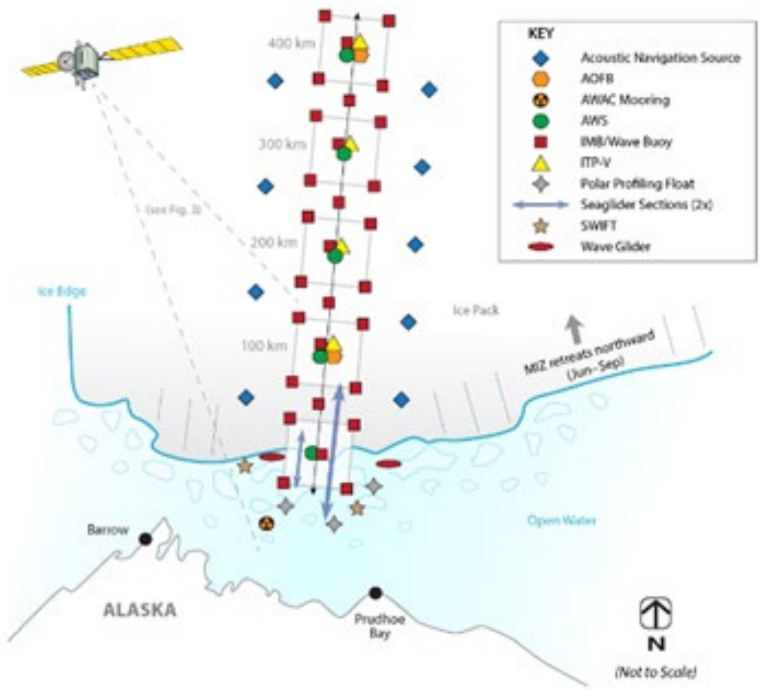

Ideal layout of ONR MIZ 2014 sensors. Each cluster center is approximately 100 km apart.

Figure 6. MIZ research project. Source: MIZ (2014).

Within the MIZ, ice mobility and open water increase toward the ice-free boundary, where open water begins. Existing analyses of the BS 2014 MIZ data set have shown the definition of a MIZ must now include the widespread thermodynamic influences within the MIZ that develop across much of the gyre at nearly the same time in late summer (Gallagher et al. 2016). In the case of the more wave-sheltered Beaufort Sea, the role of waves entering the MIZ from open ocean areas to break up the ice pack is diminished and replaced by the widespread rapid thinning of the ice pack through ice-albedo feedback, described in section E. This is in contrast to the MIZ near Greenland and Spitzbergen, which is directly influenced by high energy long fetch waves from the Atlantic.

The ONR MIZ experiment generated data timeseries from both remote sensing and ice-deployed instrument systems spanning seasonal changes from late winter to late summer 2014. During this time, the MIZ grows significantly as the ice pack thins through basal and surface melting, and eventually breaks up. As the Arctic season warms due to increased sunlight from longer days because the sun is constantly up in the summer, the

edges of solid ice transition to a MIZ, beginning as a high concentration of ice. As the summer progresses the ice pack and ocean absorb more solar radiation and trapped solar ocean heat mixes under wind driven stresses to the ice base. These thermodynamic processes continue through the summer forming a widespread MIZ. As the ice pack melts and breaks apart under thermodynamic and wind stresses, the ice concentration lowers (Figure 7). The precise dynamics of the how the MIZ develops with interactions between thermodynamics, currents, winds, and thickness of the ice pack is difficult to model (MIZ 2014).

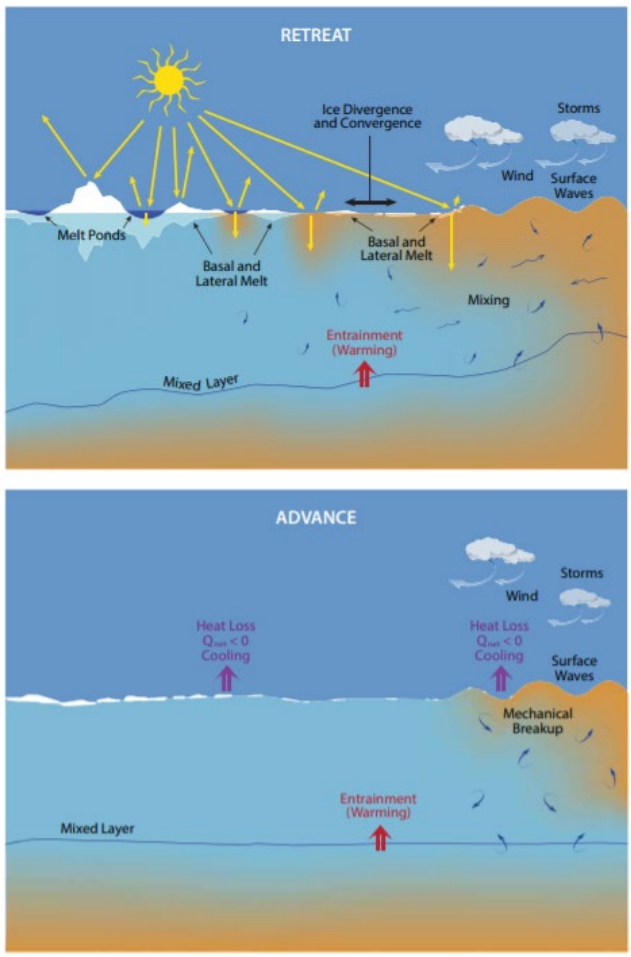

FIGURE 2. Atmosphere, ice, and upper-ocean processes governing (a) summertime sea ice retreat and (b) autumn sea ice advance. *Image credit: Kim Reading, Applied Physics Lab, University of Washington*

Figure 7. Seasonal ice retreat and advance. Source: Lee (2017).

The MIZ is a complicated region of study near the edge of the Arctic ice. Numerical models of this region are not yet able to directly capture all aspects of the small-scale physical dynamics in the MIZ. A better understanding of the interaction between wind forcing and changes in Open Water Fraction (OWF) will potentially lead to better coupled atmosphere-ice-ocean model design. A better model will increase reliability in ice concentration estimates, which may add to the forecast modeling skill in the MIZ. The representation of leads has always been difficult for numerical models to characterize (Maslowski et al. 2012). The timestep must be short because the changes in OWF occur hours to days after wind events. If the timestep is too long, then the representation of the ice field will be more flawed.

E. ICE-ALBEDO FEEDBACK

Short wave solar radiation incident on the Arctic ice pack is strongly modulated by the incident angle (angle between sunray and normal to surface), which changes with the seasonal tilt of the planet. This short-wave radiation (visible light) is the main source of heat at the Earth's poles. The sun's radiation passes through the atmosphere and is absorbed or reflected by the Earth's surface, with the reflectivity of different types of surfaces quantified by the local albedo. Albedo is a unitless quantity between 0 (fully absorbing) and 1 (white, fully reflecting) that describes how well solar energy is reflected. Albedo varies significantly between ice, water, and snow. As the sun incident angle decreases from winter to spring, snow covering the ice (with albedos around ~0.9) will begin to melt leaving ice with albedo around 0.8, while the small open water areas (leads) provide low albedo (~0.1) paths for ocean heating. As the summer progresses melt ponds develop, primarily due to snow melt on the surface of the sea ice, which further decreases the albedo (to ~0.4). This darker ice surface will then absorb more energy, transmit more solar energy to the ocean, and provide more heat for basal melting of ice floes. As the ice thins and melt ponds grow heat transfer to the ocean increases, causing more rapid thinning of the ice. Surface wind stress can overcome the plasticity of the weakening solid ice causing leads (cracks). Opening ice leads allow direct heating of the ocean, which has the lowest albedo. This positive feedback loop, known as the "Ice Albedo Feedback," rapidly increases heat available to melt ice, and the result is quickly increasing open water fraction in the ice pack.

The process continues through the summer creating large MIZ areas through thermodynamic processes and during typically light summer wind conditions. As OWF increases, the ice pack surface continues to darken, increasing the heat content in the upper ocean. During stronger wind events minor upwelling develops, changing the local energy budget of the ocean (Jackson et al. 2011, Timmermans et al. 2018). The dominant source of heat from wind-driven turbulent mixing of the upper ocean is the solar heat trapped in the upper ocean through the summer (Gallaher 2016).

In addition to the reducing albedo, there are other processes that contribute to heat arriving at the ice surface. These mechanisms include cloud and water vapor feedback (45% of total heating), and lapse rate feedback (15%). However, Ice-albedo feedback (40%) is the main contributor to the development of the MIZ, which is central to this study. Lapse rate feedback cannot be considered separate from ice-albedo processes, and together they determine Arctic temperature regulation. Studies of arctic wide albedo and clear sky albedo have shown that cloud albedo feedback does not offset the positive feedback between sea ice cover and the planet temperature increase (Perovich 2005, figure 8).

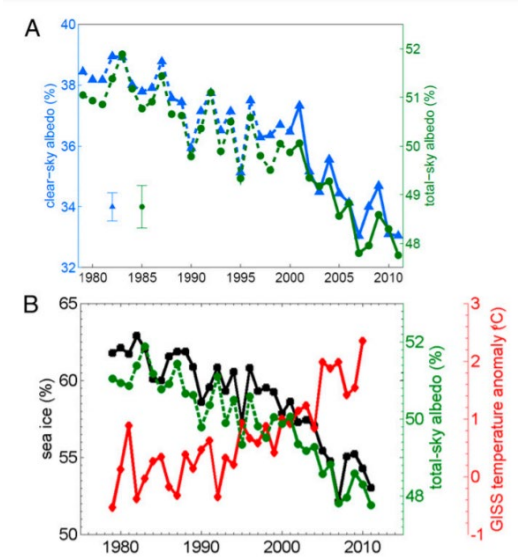

Fig. 4. (*A*) Observed annual-mean clear-sky and all-sky planetary albedo for the entire Arctic region. Solid lines are direct CERES observations, and dashed lines are estimates derived from sea ice observations. The error bars in the *Bottom Left* corner indicate the uncertainty in the pre-CERES clear-sky and all-sky albedo values (*Supporting Information*). (*B*) All-sky albedo as in *A* compared with annual-mean observed sea ice area (as a fraction of the ocean in the Arctic region) and surface air temperature averaged over the ocean in the Arctic region.

Figure 8. Observed annual mean and all sky planetary albedo for entire arctic. Source: Perovich (2005).

Observations from the 1997–1998 Surface Heat Budget of the Arctic Ocean (SHEBA) experiment showed how each season is impacted by the angle of incidence from solar radiation (Perovich 2005). In these multiyear ice pack conditions, from April to October, 68% of solar radiation was reflected to the atmosphere, while 24% was absorbed by snow and ice, and only 8% is transmitted into the ocean. In May the albedo was the greatest, therefore the largest amount of energy is reflected. June started the more rapid ice melt when 88% of solar energy enters the ocean through leads and melt ponds. The solar energy that is ultimately transmitted into the ocean reaches a maximum in August. This is when albedo and ice thickness are the smallest, with leads and melt ponds growing to their largest areas. During this August maximum, 28% of the total incoming solar radiation passes through ice and 16% (of the 28%) passes through melt ponds on ice, a significant fraction. Passive microwave satellite sensors have verified the SHEBA albedo measurements within a standard deviation (Figure 9).

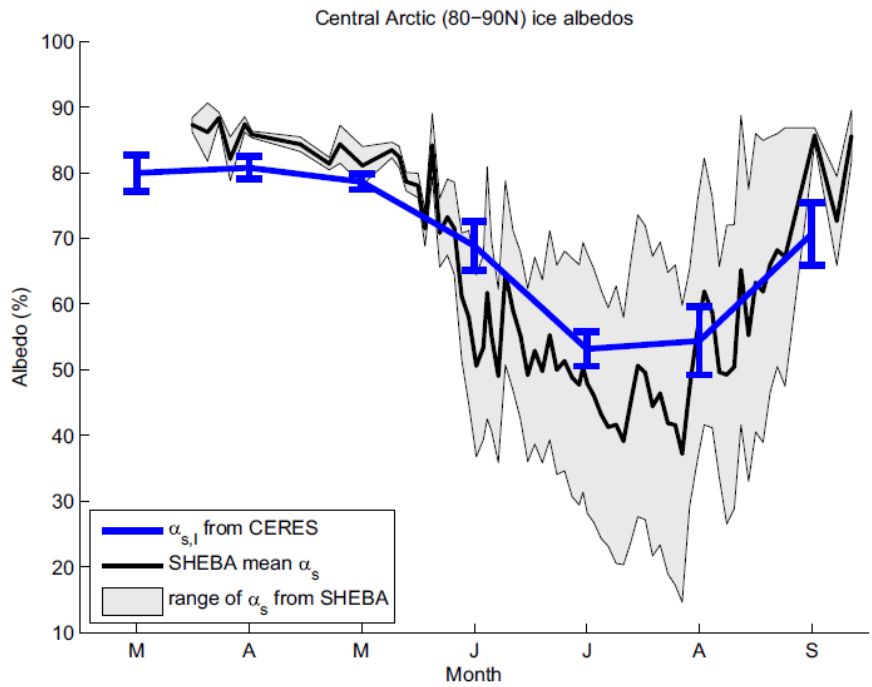

Fig. 3. The mean seasonal cycle in sea ice surface albedo during 2000–2011 derived from the CERES data in the region 80–90°N (blue line) and from in situ surface albedo measurements from the Surface Heat Budget of the Arctic (SHEBA) project (18) of 1997–1998 (black line). Blue error bars indicate one SD of CERES 2000–2011 year-to-year variability, and gray shading indicates one SD of SHEBA spatial variability along a 200-m survey line.

Figure 9. Mean seasonal cycle in sea ice albedo CERES vs. SHEBA mean. Source: Perovich (2005).

II. THESIS: RELATIONSHIPS BETWEEN ARCTIC ICE WATER FRACTION AND LOCAL 2D WIND STRESSES AT THE SURFACE OF THE CRYOSPHERE

A. INTRODUCTION OF COUPLING ATMOSPHERE TO OCEAN

This analysis will compare ice concentration in the ocean estimated from several data sets with modeled atmosphere wind stress fields. Ice concentration is defined by the fraction of ocean surface that is covered by sea ice, while OWF is (1 – ice concentration). Divergent motion in the Arctic atmosphere is thought to contribute to changes in OWF (Kwok 2002). When the wind blows, the kinetic energy and momentum of the moving atmosphere is transferred to the ice through stress in the atmospheric boundary layer above the ice pack. This analysis will use the bulk stress derived from the atmospheric forcing equation using wind components (u and v), where $\hat{u} = u + iv$.

$$\hat{\tau}_a = \rho_a C_{d_{10}} |\hat{u}_{10}| \hat{u}_{10} \tag{1}$$

This calculation results in a quadratic dependency of surface stress on mean wind speed. The thinner the ice, the faster a wind stress will accelerate it within a certain spin-up period (Brunke et al. 2006). There is a roughly linear relationship between ice drift speed and wind speed when the ice surface is solid. However, as the OWF increases in the summer, the wind-drift relationship becomes non-linear (Hibler 1981, figure 10).

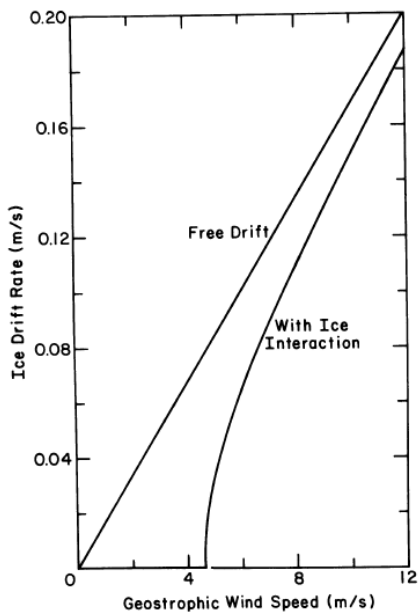

Fig. 6. Comparison of ice drift rates for an idealized one-dimensional system with and without plastic ice interaction. Quadratic boundary layers were used, and for the ice interaction case typical strength and length scales relevant to the Arctic Basin were assumed. Other constants are the same as used in Figure 3 for 3-m-thick ice.

Figure 10. Ice drift rate to Geostrophic wind speed. Source: Hibler (1981).

Wind forcing has the potential to accelerate summer melting in the MIZ, as stress transferred from the ice causes turbulent mixing within the ocean boundary layer. This turbulence readily mixes summer heat trapped in the ocean Near Surface Temperature Maximum (Gallaher et al. 2016, Timmermans et al. 2014). If the wind forcing is strong enough, the ocean turbulence reaches the base of the ocean mixed layer, and entrains heat trapped in the strongly salinity stratified winter pycnocline (Figure 11).

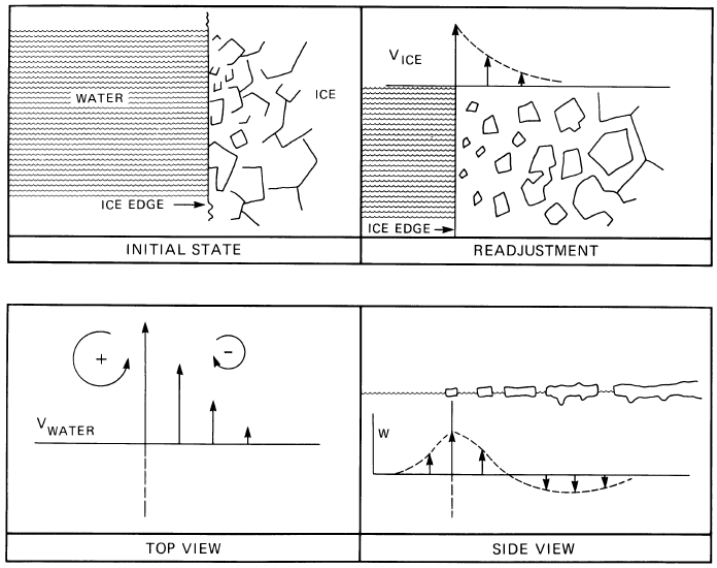

Fig. 41. Schematic diagram showing upwelling along a mobile ice edge.

Top left is the initial state of the MIZ before the ice pack breaks up. Top right is the response of ice pack as wind stress in applied North. Bottom left is the plan view of ocean surface current response as wind stress is applied North. Bottom right is the side view of the z plane of ocean current response as wind stress is applied North.

Figure 11. Upwelling near the MIZ. Source: Hibler (1981).

This pycnocline heat can come from intruding North Atlantic and North Pacific layers, but largely remains trapped by the strong stratification and very weak internal mixing (McPhee 2008, Shaw et al. 2009, Stanton et al. 2012). Well-formed Ekman spirals in both velocity and turbulent stress have been measured in the Arctic by mixed layer current profilers and turbulence sensors (McPhee 1994). The potential for vertical mixing from the pycnocline by storm induced air-ice-ocean interactions is increasingly likely with decreases in multiyear ice, increased periods of high OWF and open ocean for longer periods each year, resulting in stronger coupling of wind stress to ocean mixing. Thinner first-year sea ice is more susceptible to wind stress than older, thicker ice (Kwok et al. 2013).

Drifting ice is influenced by momentum balance between air stress (from surface winds) and water stresses (from the largely stationary deeper ocean below the pycnocline, plus small geostrophic ocean currents), internal ice stresses and ice pressure gradients. (Hibler 1981). The response of the ice to these forcing terms is controlled by ice thickness,

deformation, and compactness (Rampal et al. 2009, Spreen et al. 2011). Ice motion is forced primarily by surface wind events. If ice concentration is below 85%, surface ice stress is approximately 2% of the surface wind velocity, and 25–30 degrees to the right of surface wind direction (Nansen 1902, Mellor 1996, McPhee 1981, figure 12).

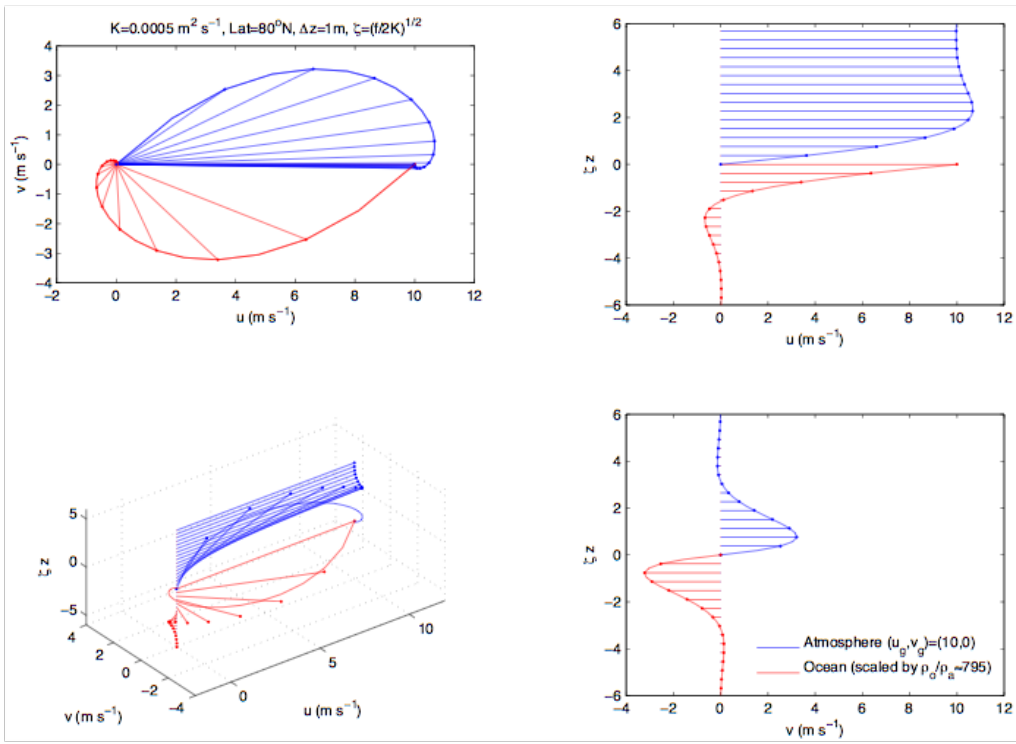

Notation	
K	vertical eddy viscosity
ζz	dimensionless Ekman layer depth

ocean magnitudes scaled to atmospheric values atmospheric heights scaled to oceanic values

Mellor, G. L., 1996: *Introduction to Physical Oceanography.* American Institutde of Physics Press, 260 pp.

Top right is the plan view of u and v wind components (blue) forcing the surface of the ocean and the Ekman response in the ocean (red). Bottom left provides a rotated view of the u and v wind components (blue) as they move through the z plane forcing a response in the ocean (red). Top right is the u wind component as it passes through the boundary layer (blue) and forces a surface response of the ocean (red). Bottom right is the v wind component as momentum is passed from the atmosphere (blue) into the ocean (red).

Figure 12. Ocean forcing. Source: Mellor (1996).

In free drift conditions widely seen away from coastal boundaries, the ice pack largely moves without lateral boundary constraints. These free drift condition extend across most of the Beaufort Sea in the summer, allowing a one-dimensional (atmospheric surface stress to ocean surface stress) approach to calculating ice movement (Omstedt et al. 1996). Consequently, local wind forcing can well predict local ice motion.

As OWF increases in the summer, surface ice accelerates more freely from wind forcing due to less friction (ice-ice interaction) among the diminishing ice pack. It is hypothesized that as the ice pack opens, the clusters of buoys will flow with the ice pack and spread apart at a similar rate as the change in OWF. The opening area in cluster buoy drift can be measured using an area divergence method (Stanton et al. 2012). This buoy area divergence over time follows changes in OWF because of area conservation of ice and will be referred to as "equivalent OWF" (eOWF). Buoy cluster eOWF can be calculated over a continuous time series and directly compared with potential forcing mechanisms including wind stress, divergence, and curl. eOWF will be compared with passive microwave Special Sensor Microwave Imager satellite (SSMI) measurements of OWF.

It is hypothesized that a correlation exists between rapid eOWF changes and wind stress events. Specifically, this analysis will test the relative contributions of local mean wind stress magnitude, wind stress direction changes, wind stress divergence, and wind stress curl to changes in eOWF (increase or decrease).

B. METHODS

1. DATA SETS

There are three primary data sources used in this analysis. The first are *in-situ* buoy positions collected during the ONR MIZ experiment. The second data set is the 2-D regional surface winds (u and v) extracted from the European Centre for Medium-Range Weather Forecasts (ECMWF) reanalysis model. The third data set is the Sea Ice Concentration data produced from the SSMI Nasa Team Algorithm.

Buoy positions from the ONR MIZ experiment have been used to produce two-dimensional drift tracks over time. The ice-deployed buoy position timeseries are determined using Global Positioning System (GPS) measurements captured every hour.

There are four clusters of buoys used in this study, with each cluster containing five buoys initially deployed approximately 10 km apart (Figure 6). These clusters of buoys drifted with the ice pack across the Beaufort Sea during 2014. The period studied in this experiment is March 21st, to September 17th, which is Year Day (YD) 80 to YD 260 during 2014. This spring-summer-fall period covered the formation of a widespread MIZ and the start of fall freeze-up at several concurrent locations covered by the buoy clusters. The buoy position accuracy is +/- 5 m, with a recorded GPS fix every hour (NPS 2014).

ECMWF ERA-Interim reanalysis model surface wind fields were extracted along the center track of each buoy cluster. Ten-meter surface wind components (u and v) were used as the wind forcing in this analysis. The model resolution of the ERA-Interim is 75 km spatial grid points, with a 1-hour sample frequency for each analysis field (ECMWF 2014).

Ice concentration is derived from the SSMI, channel F16 multispectral microwave radiometer satellite. This instrument routinely samples multispectral surface irradiance in selected microwave bands with good pan- Arctic coverage. This data is used by the NSIDC to produce an ice concentration over the surface using the NASA Team algorithm. The ice concentration field is produced 1/day with a 25 km grid spacing (NCAR 2014). Unfortunately, this data set has some weaknesses. Sea ice concentration is often under-estimate compared to observations due to cloudy weather, snow, and ice layering effects (Kwok 2002).

Despite the weaknesses of SSMI measurements, there is a long-established continuous record of gridded ice concentrations from SSMI over the Arctic and Southern Oceans for more than 40 years (Kwok 2002). These OWF/ice concentration measurements cover the entire Arctic region. This wide spatial coverage combined with the length of the data record have made SSMI an important data set for the Arctic research community. However, it is well documented that passive microwave measurements of ice concentration are not very accurate in the MIZ. Inaccuracies arise from differing surface snow conditions, melt ponds, ice thickness, changing emissivity due to ice temperatures, and atmosphere impacts such as clouds. The NASA Team algorithm reports OWF accuracy estimates with uncertainties of +/-5% (Cavalieri et al. 1984). However, comparison of seasonal

concentration changes reveal that the uncertainty increases to +/-12% during the intermediate period between winter and summer when the MIZ is most dynamic (Ivanova 2015). Atmospheric contributions, namely cloudiness, is a major contributor to uncertainty in the intermediate season (Anderson et al. 2006). The microwave sensors cannot discern between ocean water in leads and melt water over ice. Passive microwave channels near 19, 37, and 90 GHz do not penetrate water more than a few millimeters (Ulaby et al. 1986). Therefore, signals from ponds and leads appear identical within the MIZ and represent 25km square radiometer spatial averages of surface conditions that cannot resolve leads and melt ponds (Comiso 1996). Therefore, the widely varying surface conditions found in the MIZ transitioning into open ocean frequently led to misidentifying the ice edge and have large ice concentration errors.

2. ECMWF WIND FIELD STRESS, DIVERGENCE, AND CURL

In this study, ECMWF reanalysis 10m surface winds were used to calculate local bulk stress, divergence, and curl imposed on the ice pack. A local field of 10m height wind components (u and v) were extracted from the gridded model wind vectors using a bi-linear interpolation based on the center position of each buoy cluster at each one-hour time step. This process produced a Lagrangian local wind field grid that moved with each buoy cluster. The ice stress expressed in equation (1) requires surface wind components u and v, as well as the atmospheric density (ρ_a) and a selected drag coefficient (C_d). A neutral atmospheric drag coefficient of $C_d = 1.24 \times 10^{-3}$ was selected from a 2014 study in the BS (Petty 2017). Assuming a below freezing atmosphere temperature at 10m of -10°C, we employed an Arctic atmospheric density of $\rho_a = 1.35$ (kg m^{-3}) for all stress calculations. The resulting mean of the wind stress field is produced at hour intervals in units of Pascals (Pa).

Divergence of the 2-dimentional (2D) wind stress field was calculated from the extracted local wind field. For a 2D vector field of two variables (F_x and F_y), the divergence is calculated with the following equation (Figure 13). The 2-D vector field F is represented by the matrices F_x and F_y at locations X and Y.

$$div\,\boldsymbol{F} = \nabla \cdot \boldsymbol{F} = \frac{\partial F_x}{\partial x} + \frac{\partial F_y}{\partial y} \tag{2}$$

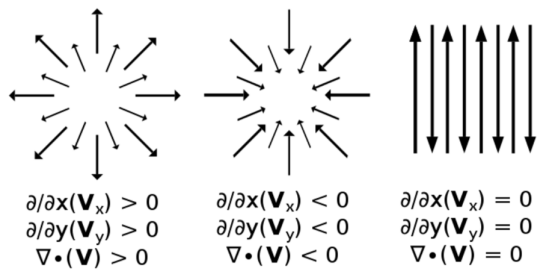

On the left, an outward 2-D vector field produces positive divergence. In the center, an inward 2-D vector field produces negative divergence. On the right, a balanced 2-D vector field produces no (zero) divergence.

Figure 13. Divergence.

Curl (Vorticity) of a 2-D wind field was calculated over the same local vector wind stress field. For a 2-D vector field of two variables, the curl (vorticity) and wind stress curl (Curl-Z) is calculated.

$$curl\,\boldsymbol{F} = \nabla \times \boldsymbol{F}\left(\frac{\partial F_y}{\partial x} - \frac{\partial F_x}{\partial y}\right)\hat{e}_i \tag{3}$$

$$\omega = \frac{1}{2}(\nabla \times \boldsymbol{F})_i = \frac{1}{2}\left(\frac{\partial F_y}{\partial x} - \frac{\partial F_x}{\partial y}\right)\hat{e}_i \tag{4}$$

The curl (vorticity) is a vector field representing the rotation speed of the stress field; measured in radians per second (rad/s) (Figure 14, left panel). The resulting wind stress curl (curl-z) is another vector field normal (perpendicular) to the surface of the ice; flux in (N/m^3) ((Figure 14, right panel). Both curl (vorticity) and wind stress curl (curl-z) may be positive or negative.

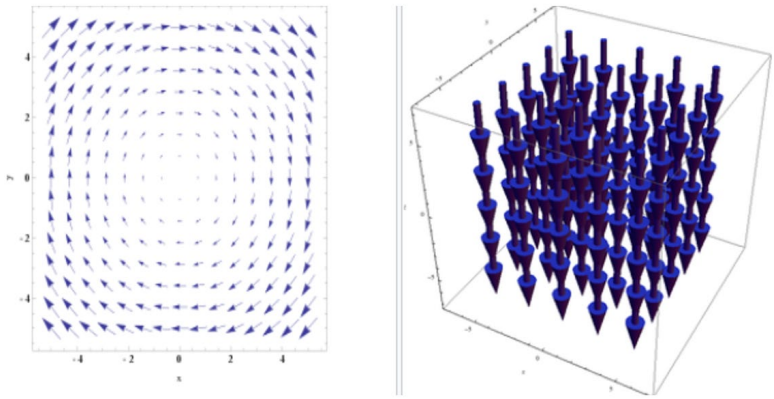

On the left, a 2-D vector field has negative curl (counterclockwise) motion. On the right, the z-plane wind stress curl response is a downward flux.

Figure 14. Curl.

3. MIZ BUOY CLUSTER eOWF

Four buoy clusters are studied in this experiment, each with five GPS tracked buoys. All cluster latitude and longitude positions were converted into Northing and Easting measurements (meters) to make trajectory and area calculations for this study. The full timeseries of the buoy cluster trajectories can be seen in Figure 15.

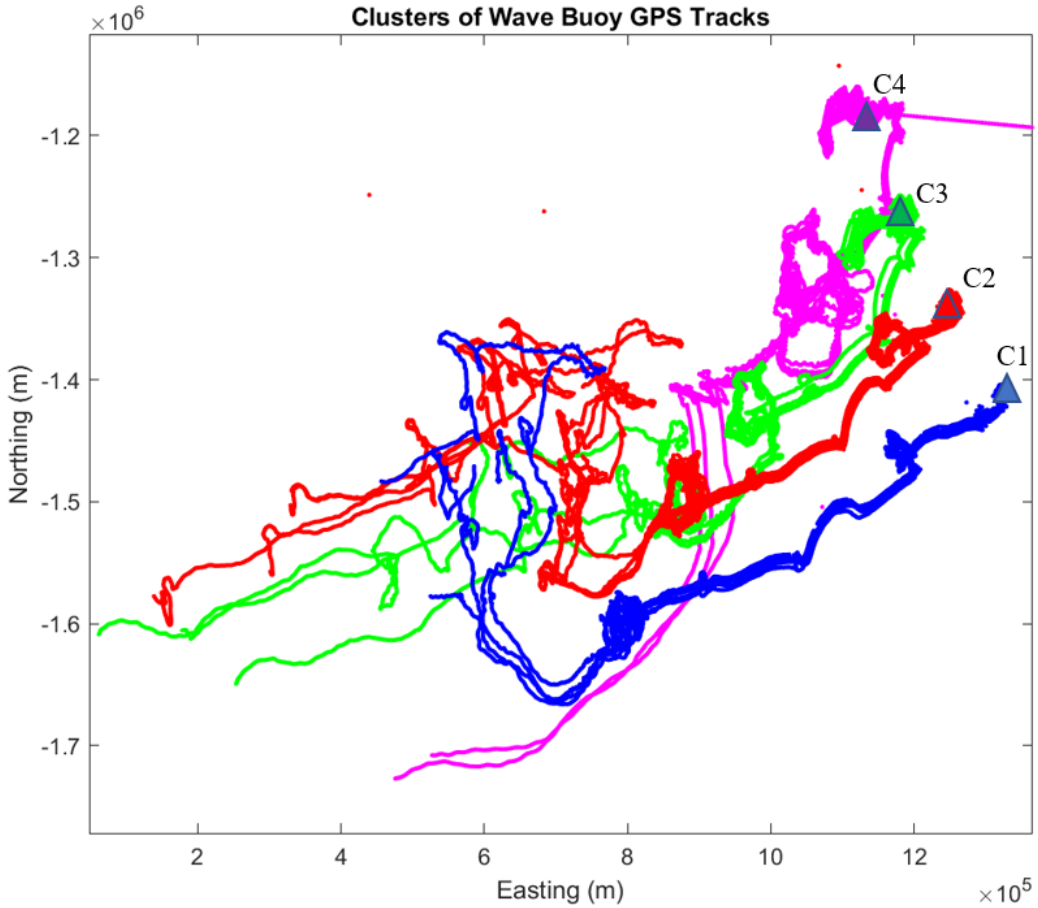

MIZ project wave buoy GPS trajectories during the spring and summer of 2014. The buoy tracks are projected in Northing and Easting (meters). The tracks begin movement from the triangle positions (100 km apart) and progress to the left over the 2014 summer. Blue tracks are Cluster 1 (C1), Red tracks are Cluster 2 (C2), Green tracks are Cluster 3 (C3), Magenta tracks are Cluster 4 (C4).

Figure 15. Buoy GPS Tracks.

Buoy clusters were deployed in the BS before the MIZ developed during March 2014. As the summer progressed and the MIZ developed, the relative position of buoys within each cluster began to change as the ice pack deformed in response to wind forcing and decreasing ice strength from basal and surface melting. The area between triplets of the five buoys within each cluster was used to calculate eOWF using all possible buoy combinations (Stanton et al. 2012). This produces ten estimates of eOWF per cluster.

$$OWF = 1 - C(t) = \big(A(t) - A_0(t)\big)/A(t) \tag{5}$$

Where $A(t)$ is the triangle area as a function of time. $A_0(t)$ is the smallest triangle area near the start of the study interval, so that $C(t)$ shows the dilution of ice as the season progresses from this most concentrated initial value. For each cluster of five buoys, the ten possible areas were calculated using equation 5 for each one-hour time step. The resulting mean of all ten area measurements is "equivalent to OWF" (eOWF). Timeseries for all clusters were calculated.

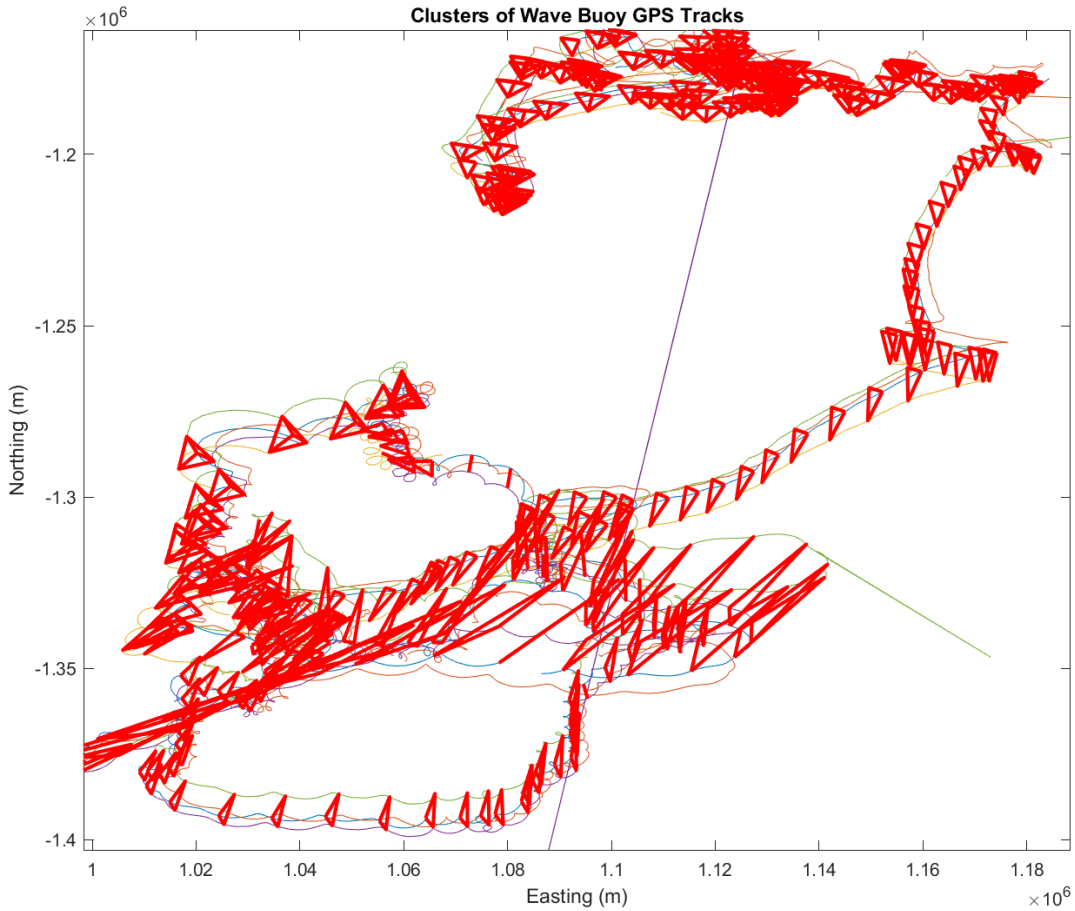

Red triangles portray the buoy combination 3–4-5, in Cluster 4. Each triangle represents a 12-hour period. The buoy tracks begin in the top right and evolve to the bottom left. There are 10 possible buoy area combinations of the 5 buoys in Cluster 4. Surface ice shear can accelerate one buoy from its sister pairs, causing an obtuse triangle. Obtuse triangles create unwanted noise in the final eOWF calculation due to wide fluctuations in area over short periods. A small angle filter removes obtuse triangle areas from the mean calculation of all ten areas within the buoy cluster. The small angle filter allows isosceles triangles to make up the majority of the eOWF calculation, promoting consistency in the final eOWF rate of change signal used in a time series.

Figure 16. Buoy area changes during seasonal drift.

Preliminary time series experiments revealed some limitations when including area calculations using small angles between buoys (Figure 16). This small angle impact arises when strong shearing events effectively remove a given buoy from its two partners. Ideally, the buoy triangles would remain largely isosceles in shape. A criterion was applied to remove small angle triangle cases from the buoy calculations. This filter prevented small angle triangles from creating nonphysical large swings in OWF (Figure 17). The stochastic nature of the eOWF signal already has significant variability, therefore filtering small angle areas allows a cleaner time series when piecewise assembly is utilized (Figure 18).

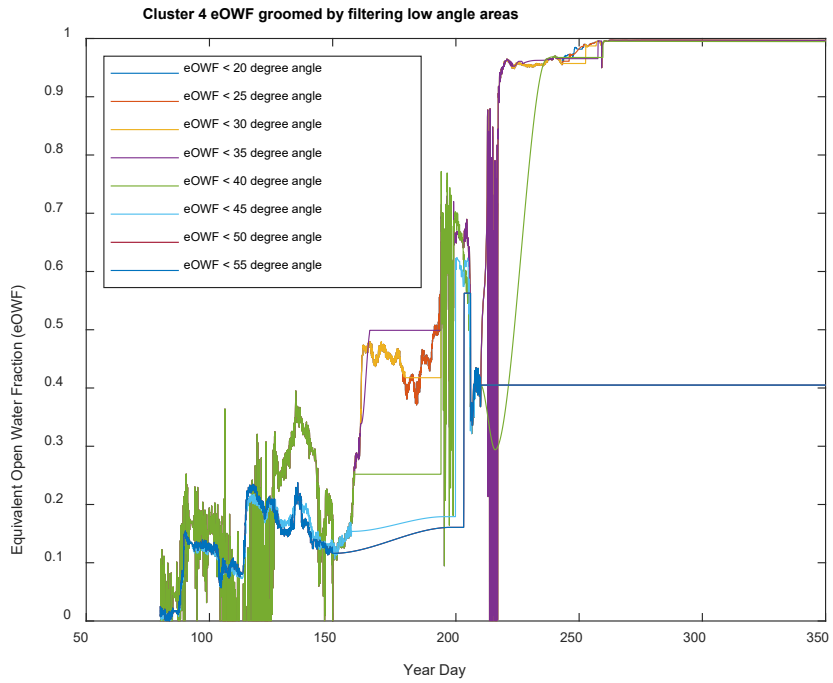

The plot shows eOWF results using a filter to remove small angle area triangles from the calculation. This process allows erroneous small angle areas to be removed, minimizing the variability in the stochastic signal. A cleaner time series is revealed for study when piece-wise assembly of the filtered eOWF is used. When small angles below 30 (yellow), 25 (orange) and 20 (blue) degrees are removed, the tolerances needed to observe a change are lower.

Figure 17. Small angle filter.

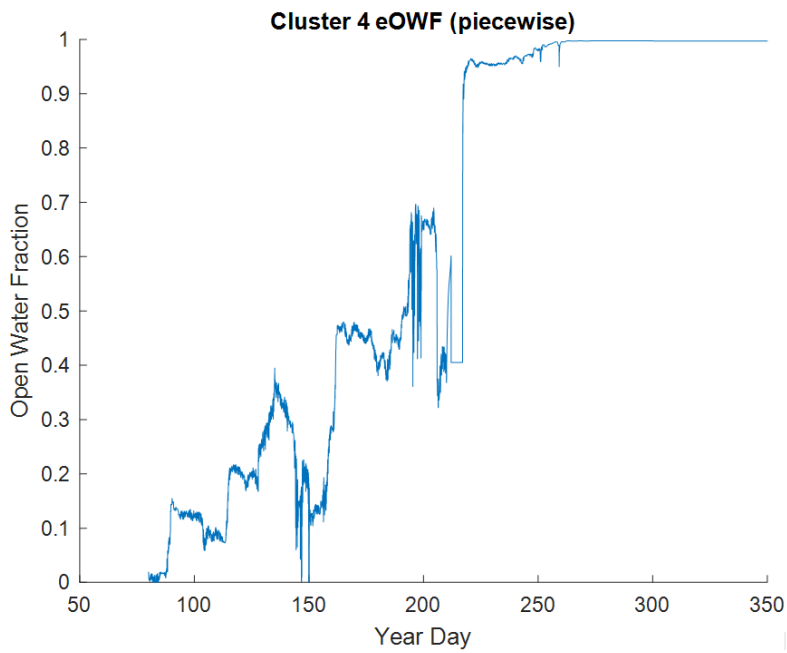

The use of a piecewise low angle filter produces a consistent final eOWF. By removing large bands of stochastic noise, the signal is ready for further analysis.

Figure 18. Piecewise eOWF.

To identify OWF 'events' the time derivative of eOWF was computed for analysis d(eOWF)/dt. The mean eOWF signal was first smoothed using a Butterworth, fourth order, low pass filer. The filter utilized a Nyquist frequency (fn) of 1/2 (hour^{-1}) and a cut off frequency (fc) of 1/12 (hour^{-1}), which produces a normalized cut of frequency of Wn = fc/ fn = 0.1667. The rate of change in eOWF was used to identify rapid eOWF change events in the remaining analyses.

4. SSMI OWF

The pan-Arctic ice concentration from SSMI was used to estimate OWF at the center position of the buoy clusters at each time step. A time series was produced using the local SSMI OWF values for analysis. The SSMI data set provides mean ice concentration estimates for each 25km square grid cell. This is equivalent to OWF by the equation OWF = 1 - C , where C is ice concentration and OWF is Open Water Fraction. OWF is measured as a value between 0 and 1, with zero being solid ice surface, and one being open ocean. eOWF is set to the same constraints, between 0 and 1 for analysis.

5. WIND DIRECTION

ECMWF provides the u and v components of the Lagrangian wind field. This allows for the calculation of wind direction utilizing the atan2 function. The use of a four-quadrant inverse tangent allows the MATLAB function atan2(Y, X), for wind components (v, u) to provide values in radians on the interval -pi to pi, in reference to the X and Y directions illustrated in Figure 19. A continuous wind direction is plotted on a time series for analysis with wind stress magnitude for analysis.

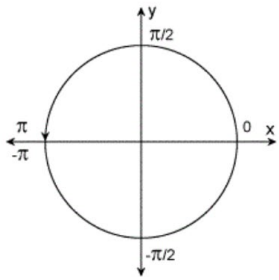

$$\operatorname{atan2}(y,x) = \begin{cases} \arctan\frac{y}{x} & x > 0 \\ \arctan\frac{y}{x} + \pi & y \geq 0, x < 0 \\ \arctan\frac{y}{x} - \pi & y < 0, x < 0 \\ +\frac{\pi}{2} & y > 0, x = 0 \\ -\frac{\pi}{2} & y < 0, x = 0 \\ \text{undefined} & y = 0, x = 0 \end{cases}$$

The use of a four-quadrant inverse tangent allows for calculation of 360-degree wind directions from u and v components.

Figure 19. Inverse tangent and atan2 function.

6. ANALYSIS TOOLS

Several analysis tools were developed to test our hypotheses including buoy position track maps, time series comparisons, Graphics Interchange Format (.gif) movies with multiple data overlays, cross correlation function, cross correlation coefficient, and normalized cross correlation. Data assimilation and analyses were conducted using MATLAB. The following general procedure outlines the analysis steps that were developed.

Some patterns, such as wind relaxation were investigated across multiple buoy clusters. The initial year-day of study was chosen as 2014080 on a Julian calendar, March 21st, 2014, after all the buoys had been deployed over a two-week period. A buoy position tracking map was produced to investigate the general layout and evolution of cluster

movement. A set of time series was produced for visual comparison using the cluster center position at every time step. The time series that are compared are eOWF, SSMI OWF, Wind Stress, Divergence, and Curl. Wind stress curl (Curl-Z) was produced in preliminary testing and found to be redundant because of the simple drag relationship used. The eOWF time series was evaluated to identify the infrequent but important large changes in OWF (within 1–2 days) that characterized these timeseries. Each change event that was identified in the eOWF was cross correlated with three time windows in the preliminary analysis. The cross-correlation window procedure is discussed in the next section. A preliminary spatial boundary test was considered in the next section to determine the best grid size for the Lagrangian wind field calculations. A cross-correlation coefficient plot with max time-lag was produced for wind stress divergence and curl using equation (6). The normalized cross-correlation coefficient (NCC) for each test was calculated using equation (7). A heat map was developed using all max-lag and NCC values for visual interpretation. Select wind events were chosen to produce movies (.gif) for presentations.

$$\widehat{R}_{xy,\mathrm{coeff}}(m) = \frac{1}{\sqrt{\widehat{R}_{xx}(0)\widehat{R}_{yy}(0)}}\widehat{R}_{xy}(m) \tag{6}$$

$$\begin{aligned}\mathrm{NCC} &= \frac{\frac{1}{mm'}\sum_{i=p}^{p+m-1}\sum_{i'=p'}^{p'+m'-1}(f_{i,i'}-\overline{f})*\cdot(g_{i+q-p,i'+q'-p'}-\overline{g})}{\sqrt{\frac{1}{mm'}\sum_{i=p}^{p+m-1}\sum_{i'=p'}^{p'+m'-1}|f_{i,i'}-\overline{f}|^2}\sqrt{\frac{1}{mm'}\sum_{i=q}^{q+m-1}\sum_{i'=q'}^{q'+m'-1}|g_{i,i'}-\overline{g}|^2}} \\ &\equiv \frac{\overline{f^*g}-(\overline{f})^*\overline{g}}{\sqrt{\overline{|f|^2}-|\overline{f}|^2}\sqrt{\overline{|g|^2}-|\overline{g}|^2}}\end{aligned} \tag{7}$$

Data timeseries from different sources in this study are reported at different time intervals. To overcome the mismatched time vectors, linear interpolation was used to produce a common 1-hour time sample for all variables. Also, due to the difficulties of collecting Arctic in-situ observations, some buoy data sets are not continuous in time, again interpolation was utilized to fill these information gaps as well.

7. TEMPORAL and SPATIAL CONSIDERATIONS

Cross correlations using 48, 96 and 144 hour timeseries tied to identified OWF events were initially evaluated. The maximum lag (maxlag) of each test was compared to determine the best sample size compared with visual inspection of these timeseries segments. Consequently, 144 hours of data previous to the OWF change events were selected to calculate cross correlations with wind stress, divergence, and curl for each event.

A time shift was used to measure the relationship between the eOWF event time and the previous wind stress over the same period. This experiment assumes that the change in the MIZ was caused by wind stress impacts that occurred prior to the eOWF event. Each cross-correlation test uses the same time length for eOWF and the wind stress. The wind stress period is shifted left, so that the end of the cross-correlation time series is the center time event for eOWF. (Figure 20)

A Time Lag (TL) was calculated by subtracting the value of the maxlag from the center time of the cross-correlation period. Since 144-hour window lengths were chosen to include previous wind stress forces, the resulting equation for this study is TL = -72 hours + maxlag.

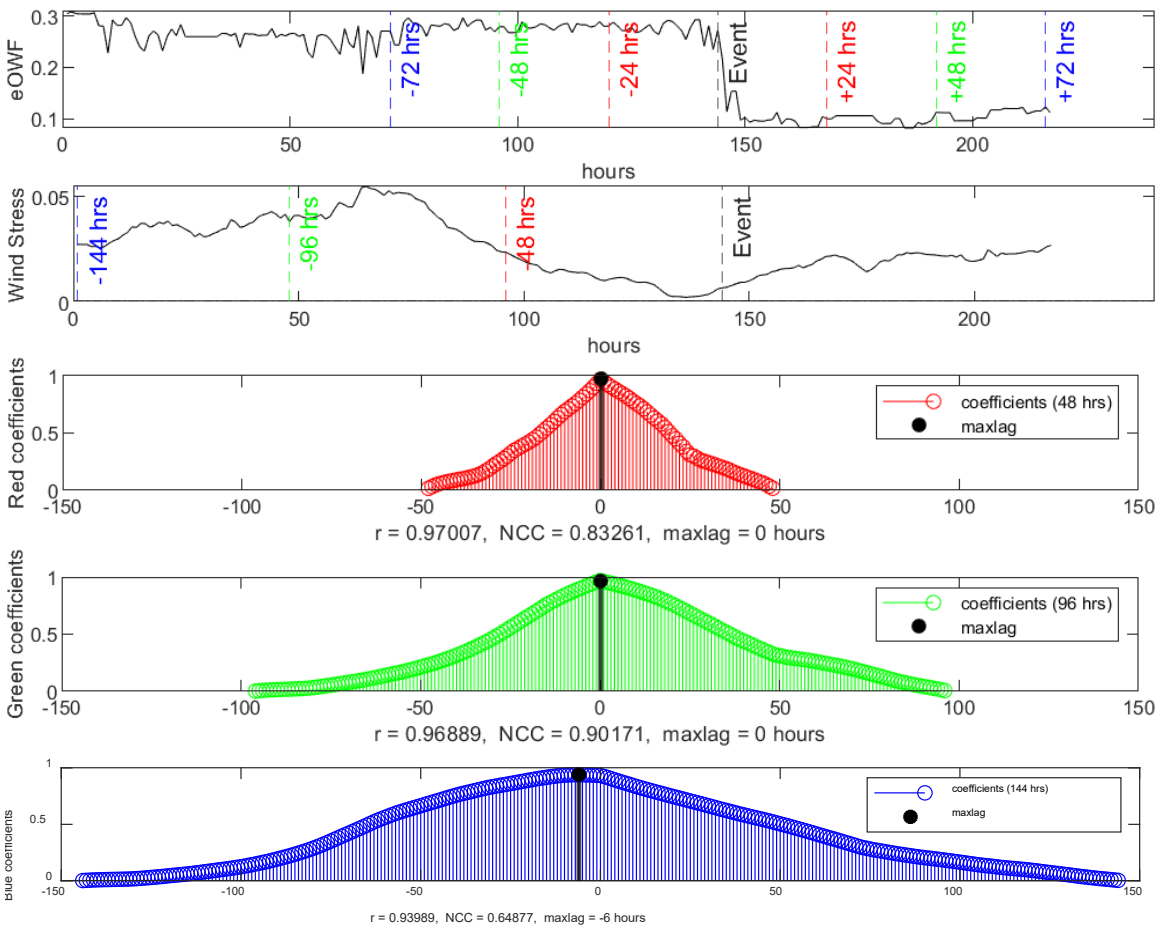

Red is eOWF +/- 24 hrs of event cross correlated with Wind Stress -48 hrs of event, Green is eOWF +/- 48 hrs of event cross correlated with Wind Stress -96 hrs of event, Blue is eOWF +/- 72 hrs of event cross correlated with Wind Stress -144 hrs of event. The -144 hr cross correlation captures the wind stress that caused the eOWF event. A -144 hr cross correlation test was selected for the remainder of this study. The wind stress period is shifted left, so that the end of the cross-correlation time series is the center time event for eOWF. Zero maxlag corresponds to half the window length time matching the time between max wind stress and the event.

Figure 20. Cross-correlation temporal test.

The choice of spatial scales for the wind stress calculations were evaluated for three spatial local grid sizes centered on the buoy cluster positions (Figure 21). The sample sizes were 3x3 grid ($3^2*75^2km^2$=50,625km^2), 5x5 grid ($5^2*75^2km^2$=140,625km^2), and 11x11 grid ($11^2*75^2km^2$=680,625km^2). (Figure 21) The variability of each was compared to determine the best sample size. Unsurprisingly, the larger grid sizes smoothed the temporal variability of the wind field, so for the remainder of this study the smallest spatial size, 3x3

grid, was selected when calculating ECMWF wind stress, divergence, and curl. The map-scale of these three local grid sizes is illustrated in (Figure 22).

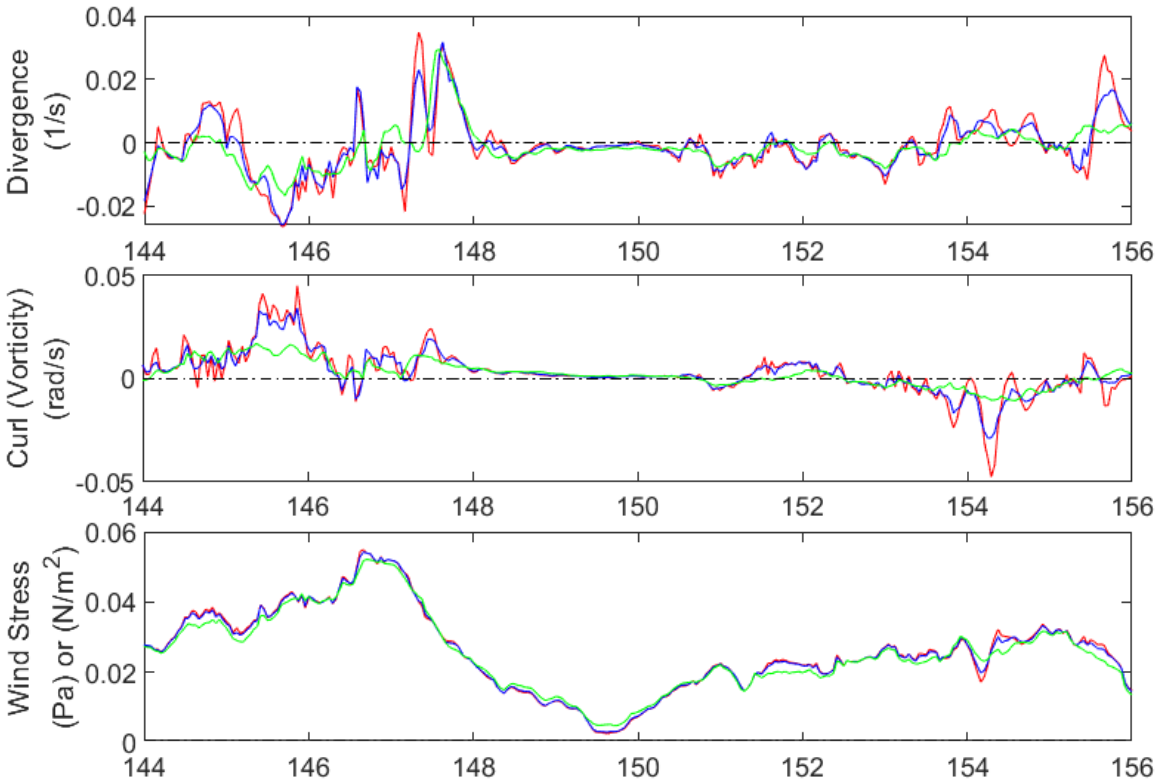

Red is 3x3 spatial grid, Blue is 5x5 spatial grid, Green is 11x11 spatial grid. Smoothing of the calculated wind stresses are observed as spatial sample size increases. A 3x3 spatial grid was selected for the remainder of this study.

Figure 21. Spatial smoothing.

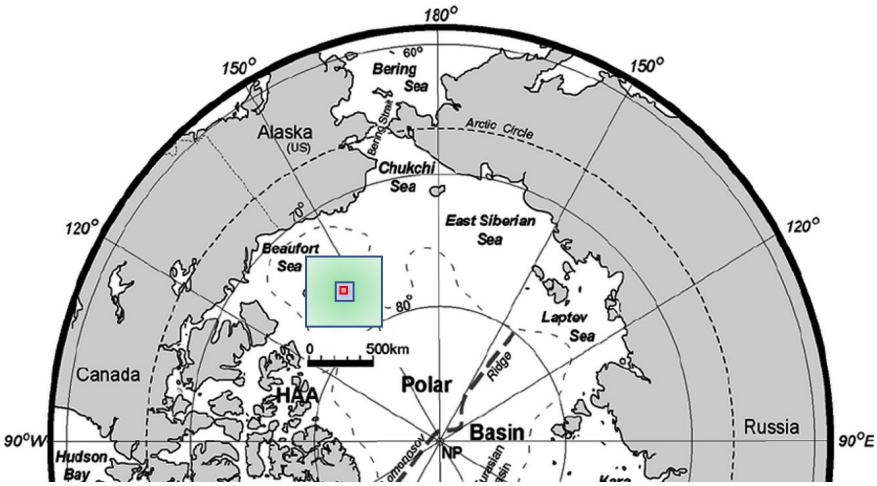

Spatial grid sizes are overlayed in the Beaufort Sea, along with a scale for perspective. Red is 3x3 grid (50,625km^2), Blue is 5x5 grid (140,625km^2), and Green is 11x11 grid (680,625km^2)

Figure 22. Spatial context.

A heat map was developed evaluating the spatial and temporal impacts on cross correlation maxlag (Figure 23). The 144-hour test results reveal it is the best period for future experiments in this study because the majority of the zero maxlag data are less than 144 hours. Additionally, the heat map illustrated how different spatial sizes did not impact the maxlag significantly. However, it should be noted that while the maxlag remained constant among the spatial tests, this does not mean that the calculated divergence and curl values will not be impacted. Smoothing remains a concern with large spatial sizes.

CLUTSER 4 maxlag							
HEAT MAP		**Temporal**					
		48 hrs	(or span=1 or Event +/-1 day)				
Spatial	Events		eO-Div	eO-Curl	eO-Stress		
9*75km^2=650km^2		Cross correlation coefficient					Mean
3x3	YD 150		3	0	3		2
3x3	YD 161		21	5	0		8.66667
3x3	YD 194		26	-1	0		8.33333
3x3	YD 206		-8	-2	0		-3.33333
	Mean		10.5	0.5	0.75		**3.91667**
25*75km^2=1875km^2							
5x5	YD 150		0	0	0		0
5x5	YD 161		0	5	0		1.66667
5x5	YD 194		0	0	0		0
5x5	YD 206		-8	-2	0		-3.33333
	Mean		-2	0.75	0		**-0.41667**
121*75km^2=9075km^2							
11x11	YD 150		-3	0	0		-1
11x11	YD 161		25	0	0		8.33333
11x11	YD 194		27	0	0		9
11x11	YD 206		12	0	0		4
	Mean		15.25	0	0		**5.08333**
CLUTSER 4 maxlag							
HEAT MAP							
		96 hrs	(or span=2 or Event +/-2 days)				
Spatial	Events	eO-SSMI	eO-Div	eO-Curl	eO-Stress	eO-WSCur	
9*75km^2=50,625kr		Cross correlation coefficient					Mean
3x3	YD 150		-30	0	-30		-20
3x3	YD 161		-27	-43	-48		-39.3333
3x3	YD 194		1	-22	0		-7
3x3	YD 206		-5	-35	-5		-15
	Mean		-15.25	-25	-20.75		**-20.3333**
25*75km^2=140,625km^2							
5x5	YD 150		-30	0	0		-10
5x5	YD 161		-24	-43	-48		-38.3333
5x5	YD 194		1	-22	0		-7
5x5	YD 206		-5	15	-5		1.66667
	Mean		-14.5	-12.5	-13.25		**-13.4167**
121*75km^2=680,625km^2							
11x11	YD 150		-21	0	0		-7
11x11	YD 161		-41	-40	-48		-43
11x11	YD 194		2	-9	0		-2.33333
11x11	YD 206		0	0	-6		-2
	Mean		-15	-12.25	-13.5		**-13.5833**
CLUTSER 4 maxlag							
HEAT MAP							
		144 hours	(or span=3 or Event +/-3 days)				
Spatial	Events		eO-Div	eO-Curl	eO-Stress		
9*75km^2=50,625kr		Cross correlation coefficient					Mean
3x3	YD 150		-29	-8	-29		-22
3x3	YD 161		-75	-91	0		-55.3333
3x3	YD 194		-43	-70	-42		-51.6667
3x3	YD 206		-53	-83	-53		-63
	Mean		-50	-63	-31		**-48**
25*75km^2=140,625km^2							
5x5	YD 150		-29	-8	-34		-23.6667
5x5	YD 161		-72	-91	0		-54.3333
5x5	YD 194		-43	-70	-42		-51.6667
5x5	YD 206		-53	-36	-53		-47.3333
	Mean		-49.25	-51.25	-32.25		**-44.25**
121*75km^2=680,625km^2							
11x11	YD 150		-21	-7	-35		-21
11x11	YD 161		-8	-88	-96		-64
11x11	YD 194		-40	-57	-41		-46
11x11	YD 206		-44	-42	-54		-46.6667
	Mean		-28.25	-48.5	-56.5		**-44.4167**

Heat map of cross correlation maxlag. The 144-hour test captures the majority of the maxlags greater than zero. This chart shows that 144 hours is the best test period to reveal future cross correlations in this study.

Figure 23. Heat map example.

C. RESULTS

Careful inspection of the spring to fall Cluster 4 timeseries reveals several patterns (Figure 24) that are illustrated in follow-on more detailed timeseries plots in figures 25–28. The X-lines in red mark the wind events studied in this cluster, (YD) 128, 150, 161, 194, and 206. Wind stress change appears to be the dominant forcing that caused an eOWF response in all these events, except YD 128, illustrated with black dashed lines in panel 4 (***B***). Wind direction shifts with wind stress; however, the wind stress magnitude (or lack thereof) appears to have more influence on eOWF than wind direction. Divergence plays an important role in the eOWF evolution over a season, shown in YD 128, 150 and 161, illustrated by black ovals in panel 1 (***A***). During times of high divergence, eOWF is in a changing mode. Divergence appears to be dominant over the impacts of curl. It is observed that curl usually acts in concert with divergence; however, divergence has higher relative amplitudes and longer wave patterns than curl. The comparison of SSMI OWF with eOWF shows that they change at the same times during the season.

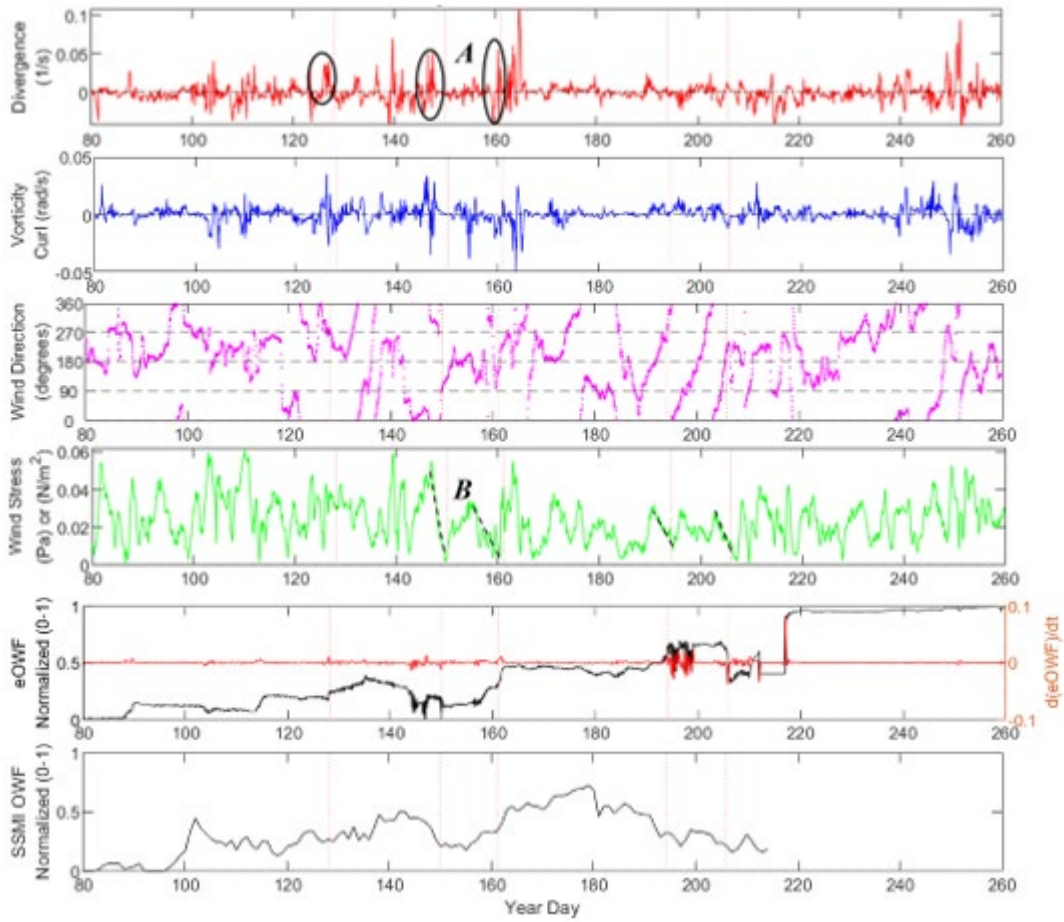

Panel 1 is Divergence, Panel 2 is Curl, Panel 3 is Wind Direction, Panel 4 is Wind Stress, Panel 5 is eOWF, with d(eOWF)/dt on the right axis, Panel 6 is SSMI OWF. All panels are displayed in Year Days (YD 80 – 260) (March 21st – Sep 17th, 2014). X-lines in red mark the wind events (YD's) studied in this cluster, (YD) 128, 150, 161, 194, and 206.

Figure 24. Annual overview of Cluster 4.

Focusing on specific eOWF divergent events allows a more detailed investigation of the forcing and OWF response (Figure 25). A convergent event is visible on YD 206 blue dashed line (***A***), as indicated by the change in eOWF in Panel 5. A pronounced decrease in d(eOWF)/dt is associated with this wind event and implies a rapidly decreasing eOWF on YD 206. A black dashed trend line (***B***) shows the relaxation period prior to the change in eOWF in panel 4. Divergence and curl are not significant in this wind event because the relaxation of wind stress is the dominant influence prior to the change in eOWF.

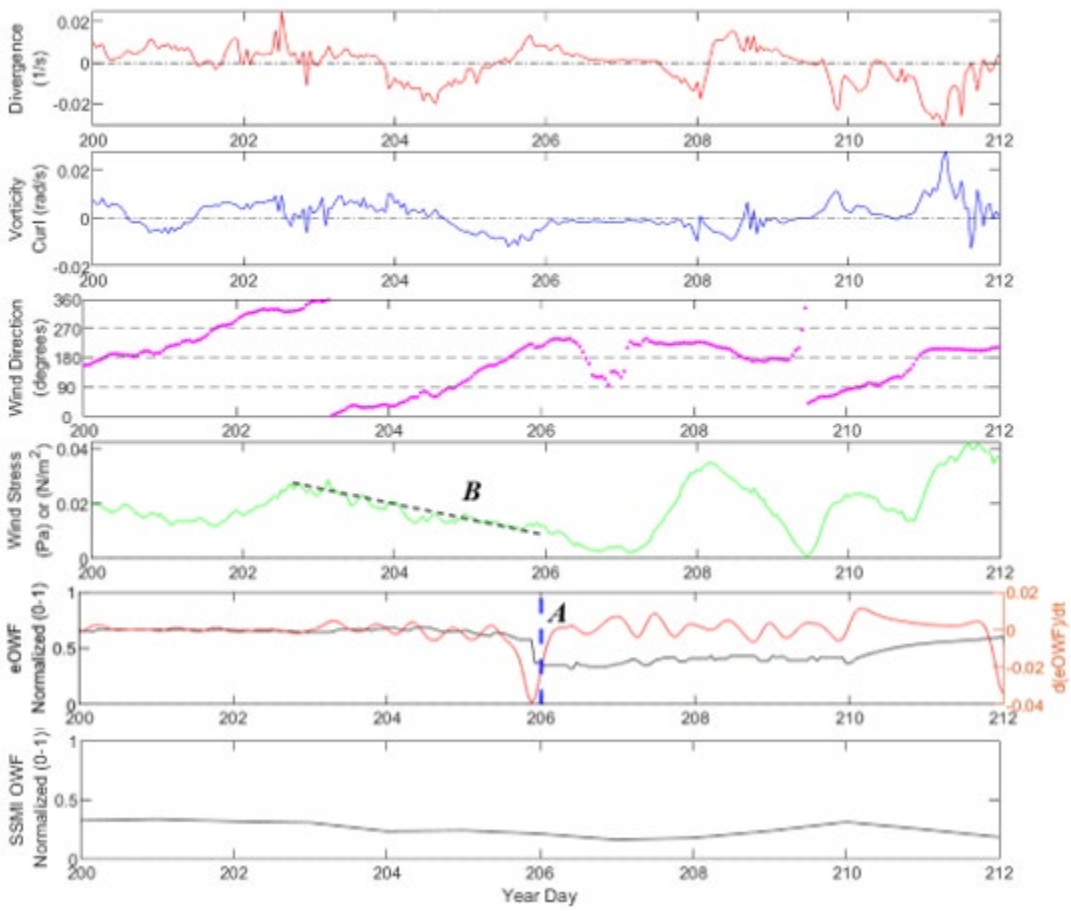

A wind event is visible on YD 206 blue dashed line, as indicated by the change in eOWF in Panel 5. A pronounced decrease in d(eOWF)/dt associated with this wind event implies a rapidly decreasing eOWF on YD 206. Panel 1 is Divergence, Panel 2 is Curl, Panel 3 is Wind Direction, Panel 4 is Wind Stress, Panel 5 is eOWF, with d(eOWF)/dt on the right axis, Panel 6 is SSMI OWF. All panels are displayed in Year Days (YD 200 – 212) (Jul 19th – Jul 31st, 2014).

Figure 25. Wind Event overview, +/-6 day (+/-144-hour) Centered on YD 206, Cluster 4.

Further inspection of the wind forcing and OWF change events shows that strong wind stress is seen prior to the majority of large eOWF changes. A repeating pattern was found of large wind stress occurrence prior to a relaxation period of very low wind stress, followed by a change in eOWF. The relaxation period is approximately 24 to 48 hours in length, and the proceeding wind stress may be continuous for days, or one large magnitude pulse over one day. After a relaxation period of about 24 hours, eOWF may change rapidly or slowly. If the relaxation period of wind stress was not changing, but the eOWF rate of change d(eOWF)/dt decreased or increased it was observed that a corresponding

intermediate period of divergence and curl occurred. There are essentially competing forces in action.

The next level of inspection involves cross correlation of the wind stresses (Figure 26). Panel 1 displays eOWF in blue and d(eOWF)/dt in red. The shaded green area shows the time series window that is used. Panel 2 provides the shaded green window for wind stress. The wind stress window is shifted prior to the wind event to study the correlation of forcing prior to the change in eOWF. Panel 3 is cross correlation coefficients in blue of eOWF and Wind Stress. A zero maxlag shows that the event occurs 72 hours after the max wind stress. Panel 4 is cross correlation coefficients in red of d(eOWF)/dt and Wind Stress. A -6 hour maxlag shows that the max rate of change in eOWF occurs at a TL of 78 hours after the dominant wind stress influence period.

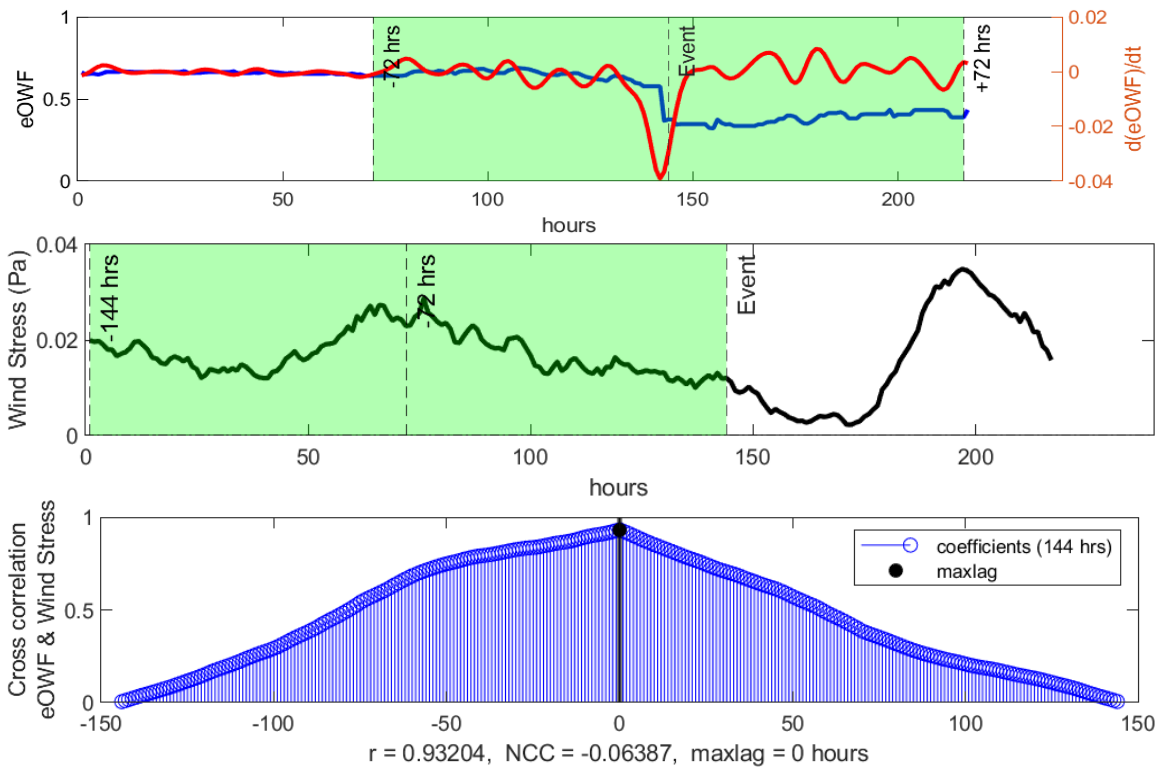

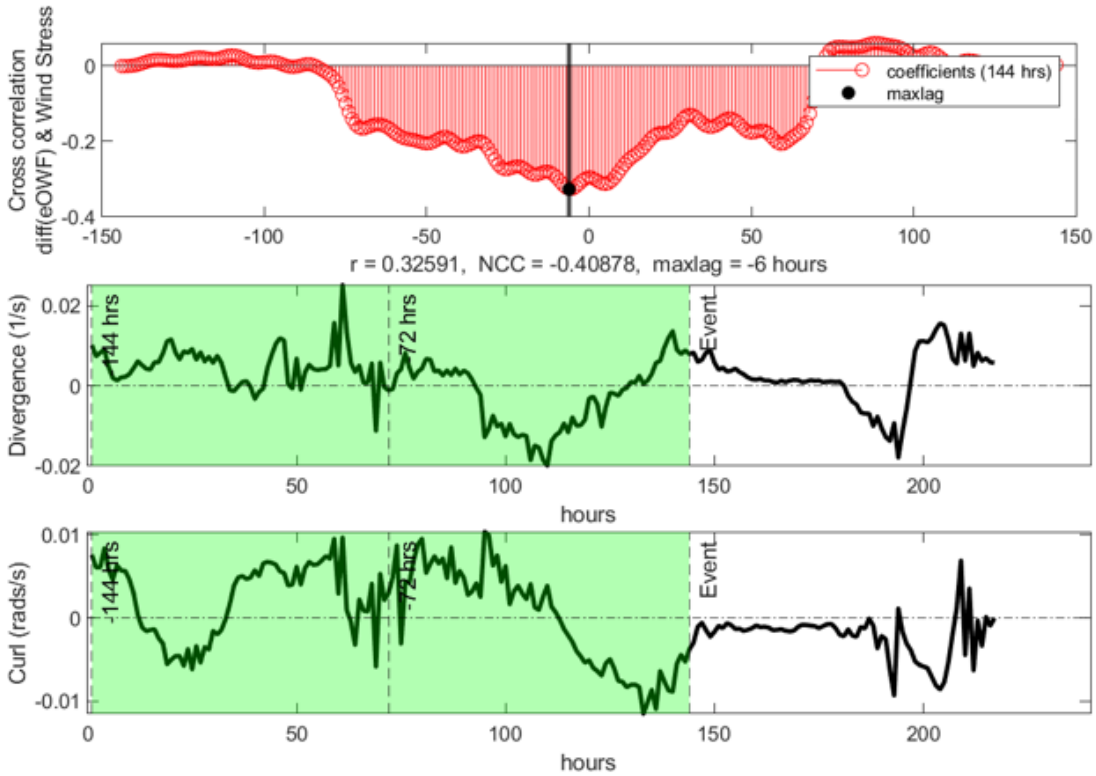

Panel 1, eOWF is blue, d(eOWF)/dt is red, window for cross correlation is shaded in green +/- 72 hours from event. Panel 2 is wind stress (Pa), window for cross correlation is shaded in green -144 hours from event, with -72 hours marked as center reference. Panel 3 is cross correlation coefficients in blue of eOWF and Wind Stress. A zero maxlag shows that the event produces a 72 hour time lag (TL) after the max wind stress. Panel 4 is cross correlation coefficients in red of d(eOWF)/dt and Wind Stress. A -6 hour maxlag shows that the max rate of change in eOWF occurs at a time lag of 78 hours after the dominant wind stress influence period. Panel 5 is divergence. Panel 6 is curl. r is cross cross-correlation coefficient, NCC is Normalized Cross Correlation, maxlag is time lag between the max values of each time series.

Figure 26. Cross correlation of eOWF and Wind Stress, YD 206, Cluster 4.

A second event is presented for study (Figure 27). A wind divergence event is visible on YD 128 blue dashed line (***A***), as indicated by the change in eOWF in Panel 5. A pronounced positive burst in d(eOWF)/dt associated with this wind event implies a rapidly increasing eOWF on YD 128. Divergence and curl are the dominant forcing in this wind event, shown by the oval shapes (***C***). After an initial jump, the eOWF increases slowly (***D***).

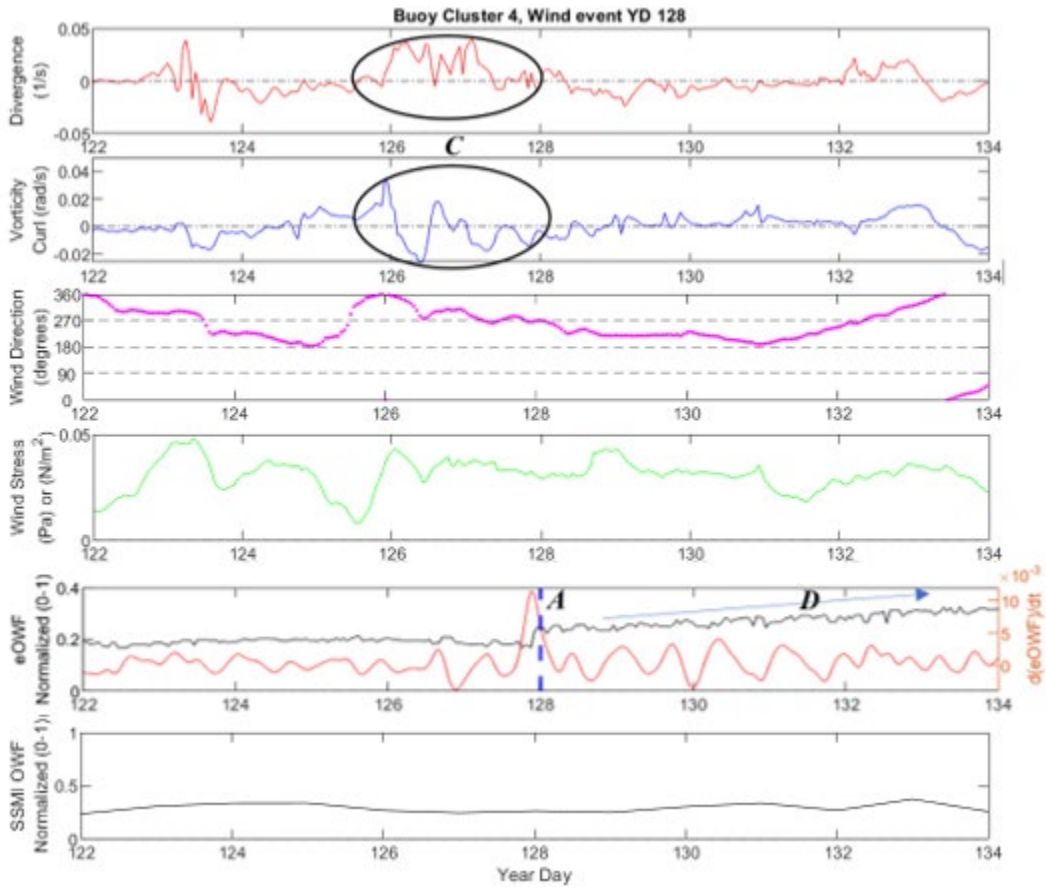

A wind event is visible on YD 128 blue dashed line, as indicated by the change in eOWF in Panel 5. This a class-II wind event, which is divergence driven, with slowly changing eOWF. Therefore, the eOWF y-axis limits are zoomed for a better view (0 - 0.4). A pronounced positive peak in d(eOWF)/dt associated with this wind event implies a rapidly increasing eOWF on YD 128 and is followed by a steady rise in eOWF for the next few days. Panel 1 is Divergence, Panel 2 is Curl, Panel 3 is Wind Direction, Panel 4 is wind stress, Panel 5 is eOWF, with d(eOWF)/dt on the right axis, Panel 6 is SSMI OWF. All panels are displayed in Year Days (YD 122 – 134) (May 2nd – May 14th, 2014).

Figure 27. Wind Event overview, +/-6 day (+/-144-hour) Centered on YD 128, Cluster 4.

The cross correlation of the divergence and curl against d(eOWF)/dt show a correlation exists, even if it is a weak r-value (Figure 28). Panel 1 displays eOWF in blue and d(eOWF)/dt in red. A -29 and -33 hour, divergence and curl maxlag shows that the max rate of change in eOWF occurs at TL 101, and 105 hours respectively. After this dominant divergence influence period, eOWF continues to increase slowly. Curl may have a greater r-value but the divergence signal is sustained for a longer period showing this event is a divergence forced event.

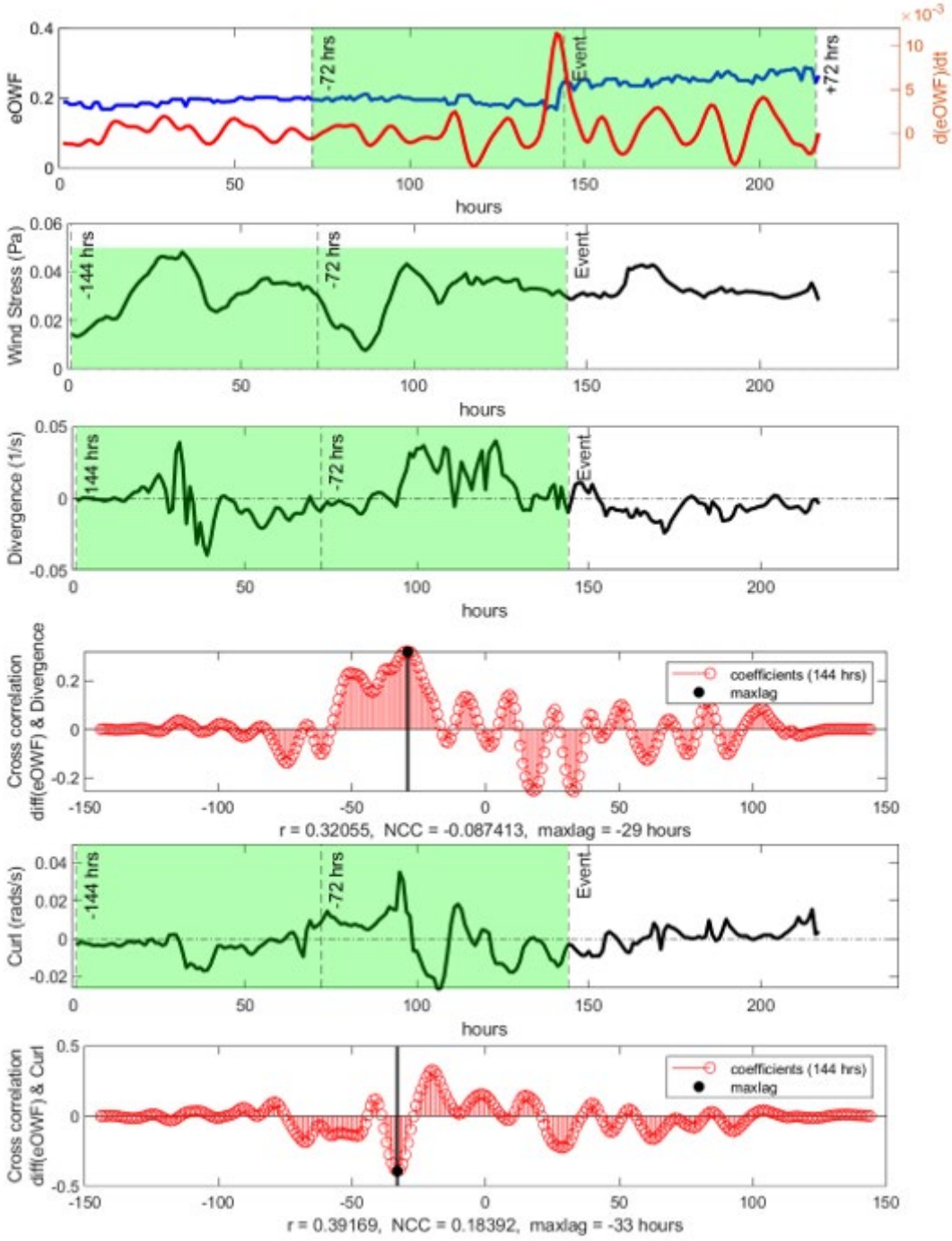

Panel 1, eOWF is blue, d(OWF)/dt is red, window for cross correlation is shaded in green +/- 72 hours from event. Panel 2 is wind stress (Pa), window for cross correlation is shaded in green -144 hours from event, with -72 hours marked as center reference. Panel 3 is divergence. Panel 4 is cross correlation coefficients in red of d(eOWF)/dt and divergence. Panel 5 is Curl. Panel 6 is cross correlation coefficients in red of d(eOWF)/dt and curl. r is cross correlation coefficient, NCC is Normalized Cross Correlation, maxlag is time lag between the max values of each time series.

Figure 28. Cross correlation of eOWF with Divergence, and Curl, YD 128, Cluster 4.

The events identified for study in Cluster 1 are Year Day (YD) 119, 126, 143, 195, 215) (Figure 29). The remaining event studies and data are available in the appendix. Again, we see that wind stress change appears to be the dominant forcing that causes an eOWF response, illustrated with black dashed lines in panel 4 (***B***). Divergence plays a primary role in YD 143, illustrated by a black oval in panel 1 (***A***). Divergence remains dominant over the impacts of curl shown in panel 2.

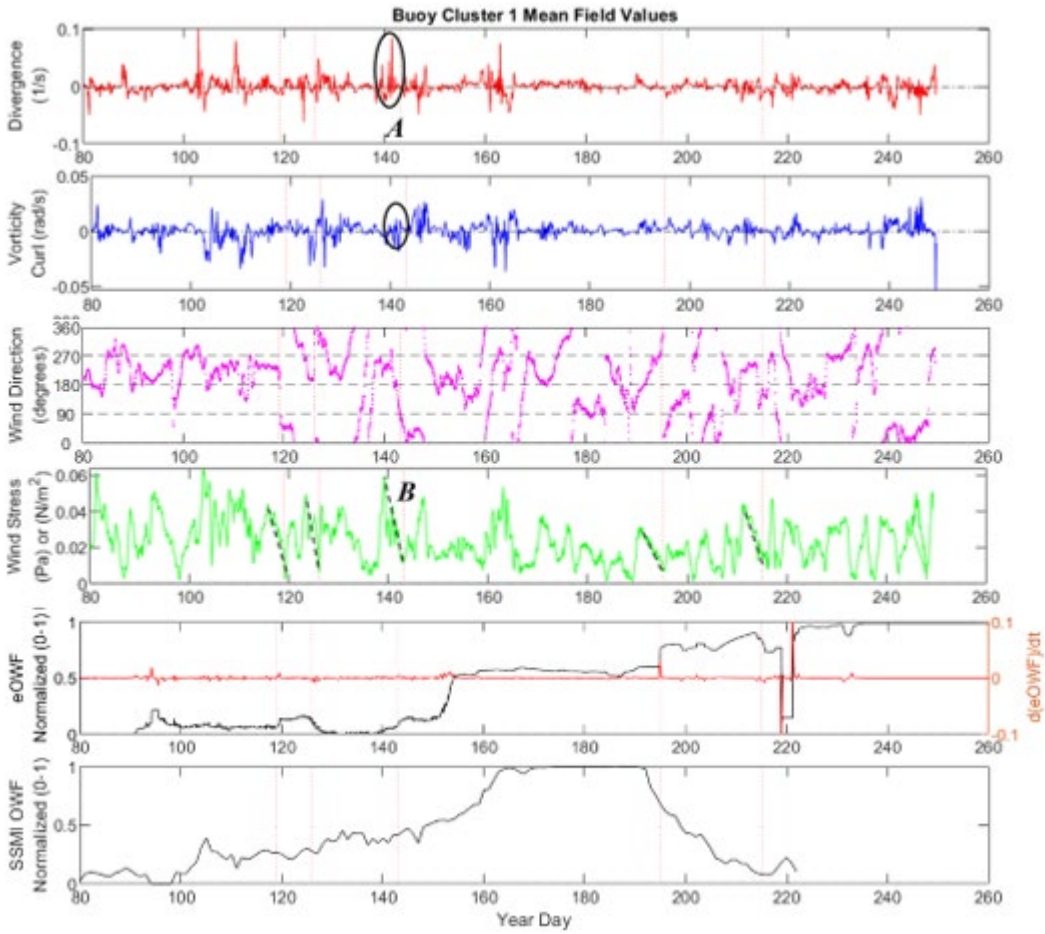

Panel 1 is Divergence, Panel 2 is Curl, Panel 3 is Wind Direction, Panel 4 is Wind Stress, Panel 5 is eOWF, with d(eOWF)/dt on the right axis, Panel 6 is SSMI OWF. All panels are displayed in Year Days (YD 80 – 260) (March 21st – Sep 17th, 2014). Studied wind events are highlighted in red X-lines, (YD) 119, 126, 143, 195, 215.

Figure 29. Annual overview of Cluster 1.

We now narrow in on YD 119 to present another wind stress relaxation response (Figure 25). A blue dashed line shows the eOWF response in panel 5 (***A***). A pronounced increase in d(eOWF)/dt associated with this wind event implies a rapidly increasing eOWF on YD 119. A black dashed trend line (***B***) shows the relaxation period prior to the change in eOWF in panel 4. Divergence and curl are not influential in this wind event because they are not the dominant forcing during the wind stress relaxation period. There is a lack of wind stress forcing during the relaxation period just before the change in eOWF occurs.

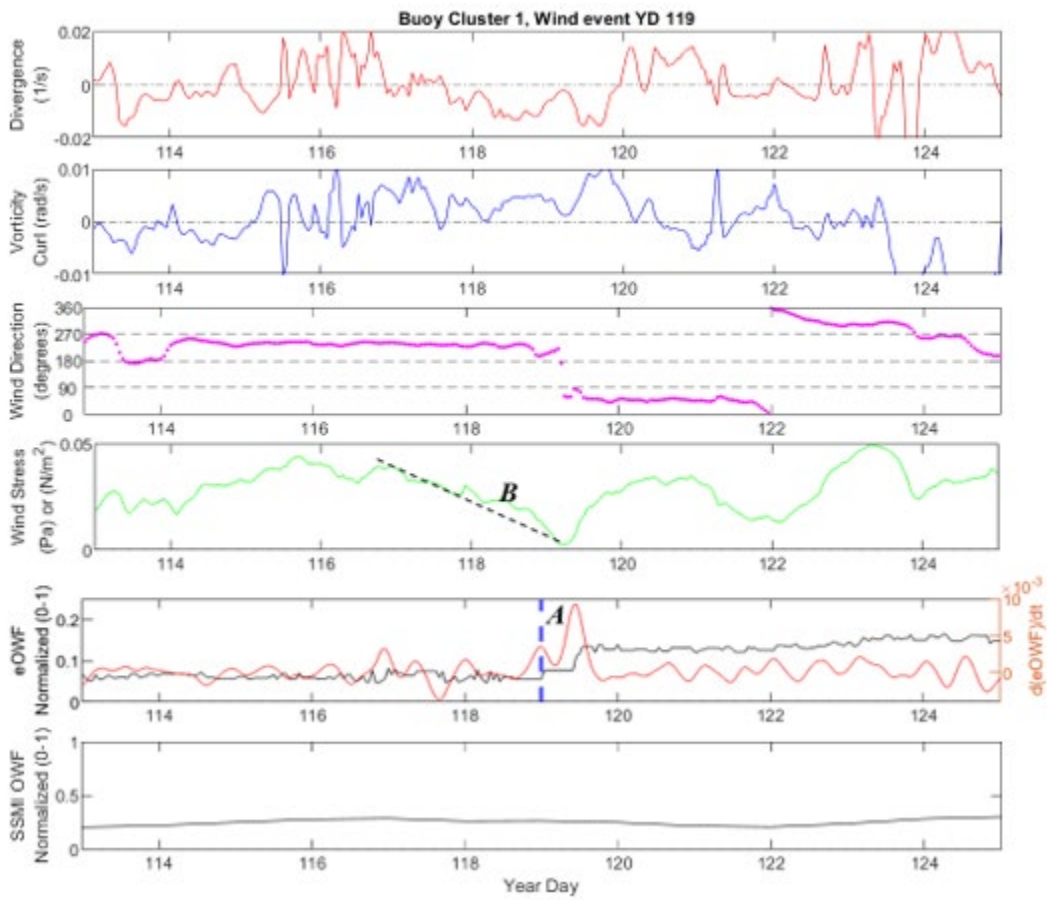

A wind event is visible on YD 119 blue dashed line, as seen from the change in eOWF in Panel 5. A pronounced positive d(eOWF)/dt increase associated with this wind event implies a rapidly increasing eOWF on YD 119. Panel 1 is Divergence, Panel 2 is Curl, Panel 3 is Wind Direction, Panel 4 Wind Stress, Panel 5 is eOWF, with d(eOWF)/dt on the right axis, Panel 6 is SSMI OWF. All panels are displayed in Year Days (YD 113 – 225) (Apr 23rd – May 5th, 2014).

Figure 30. Wind Event overview, +/-6 day (+/-144-hour) Centered on YD 119, Cluster 1.

The cross correlation coefficients for eOWF and wind stress are in blue, panel 3 (Figure 31). The cross correlation coefficients in red are d(eOWF)/dt and wind stress, panel 4. A 19 hour maxlag shows that the highest rate of change in eOWF occurs at a TL of 53 hours after the dominant wind stress influence period. A 16 hour maxlag shows that the highest rate of change in d(eOWF)/dt occurs at a TL of 56 hours after the dominant wind stress influence period.

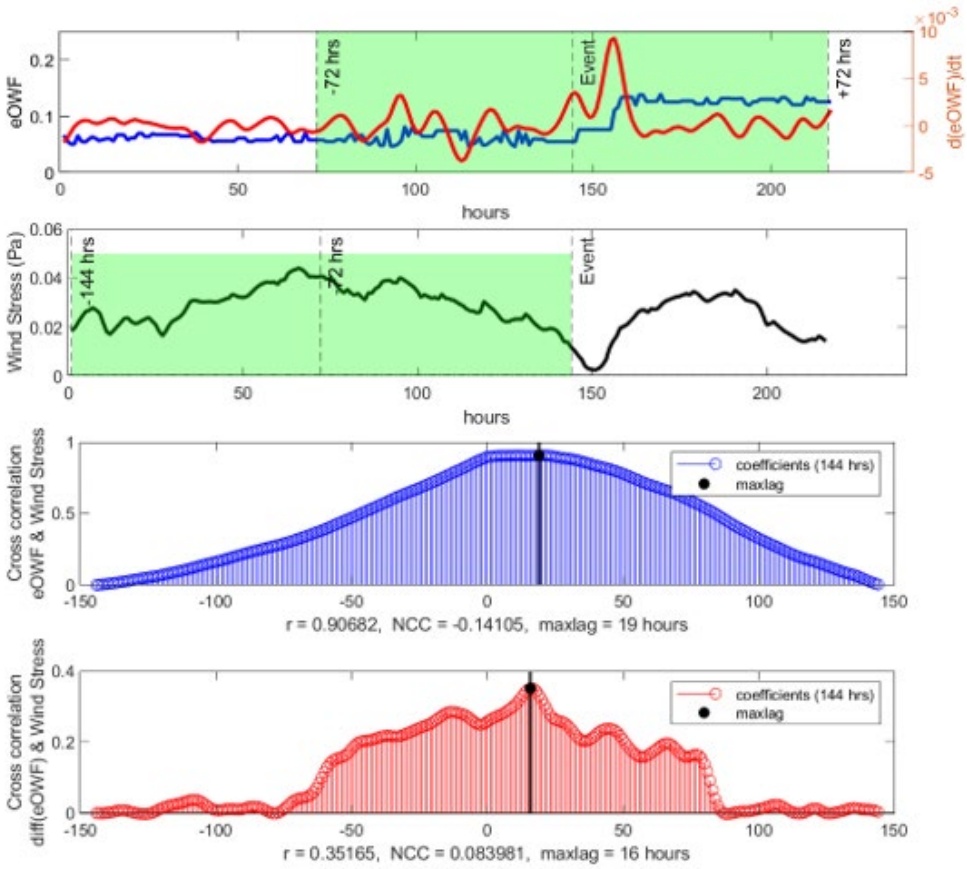

Panel 1, eOWF is blue, d(OWF)/dt is red, window for cross correlation is shaded in green +/- 72 hours from event. Panel 2 is wind stress (Pa), Panel 3 is cross correlation coefficients in blue of eOWF and Wind Stress. A 19 hour maxlag shows that the event has a TL of 53 hours after the max Wind Stress. Panel 4 is cross correlation coefficients in red of d(eOWF)/dt and Wind Stress. A 16 hour maxlag shows that the max rate of change in eOWF has a TL of 56 hours after the dominant wind stress influence period. r is cross correlation coefficient, NCC is Normalized Cross Correlation, maxlag is time lag between the max values of each time series.

Figure 31. Cross correlation of eOWF and Wind Stress, YD 119, Cluster 1.

Heat map tables were used to evaluate all data collected for Cluster 1 and 4 (Figures 32 and 33). A review of the data tables shows that wind stress has a very strong cross correlation coefficient (r-value) with eOWF. Additionally, divergence and curl appear to be secondary forces compared to wind stress. Curl has a higher r-value than divergence in both clusters. However, when NCC is considered, divergence is more influential. The NCC is used to determine the most influential secondary force because NCC normalizes by magnitude allowing different forces to be compared. The mean TL for Cluster 4 using all wind forcing values (wind stress, divergence, and curl) for both eOWF and d/(eOWF)/dt is 13 hours. The mean TL for Cluster 1 using all wind stresses (wind stress, divergence and curl) for both eOWF and d/(eOWF)/dt is 71 hours. The TL represent the average length of one entire relaxation period from the maximum wind stress forcing, to a very low wind stress (or no wind stress in some cases), culminating in the moment of highest rate of change in eOWF. The mean TL of only wind stress in Cluster 4 is very close to Cluster 1. The wind stress TL for both eOWF and d/(eOWF)/dt in Cluster 4 is 75 hours. The wind stress TL for both eOWF and d/(eOWF)/dt in Cluster 1 is 62.5 hours. These wind stress TL values will be explored in the next section.

CLUTSER 4 Xcorr 'r'		eOWF & Stress			
		eOWF-WS	eOWF-Div	eOWF-Curl	
Events	YD 128	0.94453	0.28935	0.21377	
	YD 150	0.91182	0.3	0.49241	
	YD 161	0.82525	0.16809	0.54672	
	YD 194	0.94371	0.29288	0.71104	
	YD 206	0.93204	0.31237	0.36031	
	Mean	0.91147	0.27254	0.46485	0.54962

CLUTSER 4 Xcorr 'r'		d(eOWF)/dt & Stress			
		eOWF-WS	eOWF-Div	eOWF-Curl	
Events	YD 128	0.27877	0.32055	0.39169	
	YD 150	0.22505	0.35216	0.35686	
	YD 161	0.5651	0.39619	0.41755	
	YD 194	0.19021	0.35137	0.30952	
	YD 206	0.32591	0.50945	0.43275	
	Mean	0.31701	0.38594	0.38167	0.36154

CLUTSER 4 NCC		eOWF & Stress			
		eOWF-WS	eOWF-Div	eOWF-Curl	
Events	YD 128	0.05482	0.43843	0.04511	
	YD 150	0.44874	0.21915	0.13703	
	YD 161	0.25616	0.16844	0.41755	
	YD 194	0.25787	0.21155	0.17106	
	YD 206	0.06387	0.46037	0.08258	
	Mean	0.21629	0.29959	0.17067	0.22885

CLUTSER 4 NCC		d(eOWF)/dt & Stress			
		eOWF-WS	eOWF-Div	eOWF-Curl	
Events	YD 128	0.09927	0.08741	0.18392	
	YD 150	0.29309	0.11565	0.06214	
	YD 161	0.01014	0.16912	0.07894	
	YD 194	0.09508	0.10333	0.05549	
	YD 206	0.40878	0.10826	0.03268	
	Mean	0.18127	0.11675	0.08263	0.12689

CLUTSER 4 maxlag		eOWF & Stress			
		eOWF-WS	eOWF-Div	eOWF-Curl	
Events	YD 128	0	-94	78	
	YD 150	0	-55	9	
	YD 161	0	24	7	
	YD 194	0	-43	18	
	YD 206	0	51	-34	
	Mean	0	-23.4	15.6	-2.6

CLUTSER 4 maxlag		d(eOWF)/dt & Stress			
		eOWF-WS	eOWF-Div	eOWF-Curl	
Events	YD 128	36	-29	-33	
	YD 150	4	-84	20	
	YD 161	-52	-23	-29	
	YD 194	-12	68	7	
	YD 206	-6	-39	-65	
	Mean	-6	-21.4	-20	-15.8

CLUTSER 4 TL		eOWF & Stress			
		eOWF-WS	eOWF-Div	eOWF-Curl	
Events	YD 128	-72	166	6	
	YD 150	-72	127	63	
	YD 161	-72	-48	-65	
	YD 194	-72	-115	-54	
	YD 206	-72	-21	106	
	Mean	-72	21.8	11.2	-13

CLUTSER 4 TL		d(eOWF)/dt & Stress			
		eOWF-WS	eOWF-Div	eOWF-Curl	
Events	YD 128	-36	-101	-105	
	YD 150	-68	-84	-52	
	YD 161	-124	-95	-101	
	YD 194	-84	-4	-65	
	YD 206	-78	-111	-137	
	Mean	-78	-79	-92	-83

This heat map table represents all data collected for Cluster 4. The cross-correlation coefficient "r," Normalized Correlation Coefficient (NCC), maxlag, and time lag (TL) = (-72+(maxlag)) is provided. The first column of tables uses eOWF. The second column of tables uses d(eOWF)/dt, which is specifically used to better capture the maxlag and TL. The heat map colors present the highest values for each table in green, the lowest in red, and shades the relative range in between the max/min with yellow.

Figure 32. Data heat map, Cluster 4.

CLUTSER 1 Xcorr 'r'		eOWF & Stress			
		eOWF-WS	eOWF-Div	eOWF-Curl	
Events	YD 119	0.90682	0.26197	0.47736	
	YD 126	0.81138	0.19464	0.42341	
	YD 143	0.886035	0.30748	0.45088	
	YD 195	0.91642	0.50432	0.70889	
	YD 215	0.92245	0.39668	0.37139	
	Mean	0.888621	0.333018	0.486386	0.569342

CLUTSER 1 Xcorr 'r'		d(eOWF)/dt & Stress			
		eOWF-WS	eOWF-Div	eOWF-Curl	
Events	YD 119	0.35165	0.36137	0.41476	
	YD 126	0.45812	0.26097	0.51143	
	YD 143	0.47129	0.38386	0.477029	
	YD 195	0.37259	0.71045	0.48991	
	YD 215	0.50557	0.40505	0.38411	
	Mean	0.431844	0.42434	0.455448	0.437211

CLUTSER 1 NCC		eOWF & Stress			
		eOWF-WS	eOWF-Div	eOWF-Curl	
Events	YD 119	0.14105	0.15269	0.56754	
	YD 126	0.10786	0.16021	0.20524	
	YD 143	0.14038	0.23954	0.093363	
	YD 195	0.32368	0.5965	0.056664	
	YD 215	0.12116	0.062017	0.21193	
	Mean	0.166826	0.242191	0.226947	0.211988

CLUTSER 1 NCC		d(eOWF)/dt & Stress			
		eOWF-WS	eOWF-Div	eOWF-Curl	
Events	YD 119	0.083981	0.33695	0.073369	
	YD 126	0.40542	0.089134	0.21475	
	YD 143	0.006178	0.34911	0.009385	
	YD 195	0.15055	0.12451	0.1076	
	YD 215	0.60415	0.010375	0.035981	
	Mean	0.250056	0.182016	0.088217	0.17343

CLUTSER 1 maxlag		eOWF & Stress			
		eOWF-WS	eOWF-Div	eOWF-Curl	
Events	YD 119	19	-9	-1	
	YD 126	-54	0	-50	
	YD 143	26	60	-30	
	YD 195	0	75	-15	
	YD 215	0	-20	13	
	Mean	-1.8	21.2	-16.6	0.933333

CLUTSER 1 maxlag		d(eOWF)/dt & Stress			
		eOWF-WS	eOWF-Div	eOWF-Curl	
Events	YD 119	16	-48	-20	
	YD 126	0	9	-4	
	YD 143	25	-1	-32	
	YD 195	31	46	22	
	YD 215	-8	-52	42	
	Mean	12.8	-9.2	1.6	1.733333

CLUTSER 1 TL		eOWF & Stress			
		eOWF-WS	eOWF-Div	eOWF-Curl	
Events	YD 119	-53	-81	-73	
	YD 126	-126	-72	-122	
	YD 143	-46	-12	-102	
	YD 195	-72	3	-87	
	YD 215	-72	-92	-59	
	Mean	-73.8	-50.8	-88.6	-71.0667

CLUTSER 1 TL		d(eOWF)/dt & Stress			
		eOWF-WS	eOWF-Div	eOWF-Curl	
Events	YD 119	-16	-120	-92	
	YD 126	-72	-63	-76	
	YD 143	-47	73	-104	
	YD 195	-41	-26	-50	
	YD 215	-80	-124	30	
	Mean	-51.2	-52	-58.4	-53.8667

This heat map table represents all data collected for Cluster 1. The cross-correlation coefficient "r," Normalized Correlation Coefficient (NCC), maxlag, and time lag (TL) = (-72 + (maxlag)) is provided. The first column of tables uses eOWF. The second column of tables uses d(eOWF)/dt, which is specifically used to better capture the maxlag and TL. The heat map colors present the highest values for each table in green, the lowest in red, and shades the relative range in between the max/min with yellow.

Figure 33. Data heat map, Cluster 1.

D. DISCUSSION

After studying all the divergence events for Cluster 4 and 1, we determine that they can be broken into two classes. The first type of event (class-I) is a strong wind stress period followed by a weak wind stress, called a relaxation period. The relaxation period appears to be the precursor to a coming sharp change in eOWF. This rapid, large change in the eOWF is the defining description of the class-I wind events (for example, Figure 26, panels 1 and 2). The second type (class-II) of event involves a slowly changing eOWF. The slow change is preceded by a moderate change in wind stress; however, the relaxation period is not continuous. As eOWF slowly changes, periods of increased divergence drive

short, small bursts of d(eOWF)/dt, followed by a slow change in eOWF over an extended time. The appearance of divergence with a moderate wind stress is the defining description of the class-II wind events (for example Figure 28 panels 1,3, and 5).

The class-I type of wind event is more common and is easily identifiable in the eOWF timeseries with a prominent change in eOWF, illustrated by the rate of change in d(eOWF)/dt. The class-II (divergence) wind events appear in 20% of the identified eOWF events. These high positive (divergent) and negative (convergent) wind events do not necessarily have very high mean wind stresses. Conversely, the class-I events have much less divergence seen in the timeseries. It must be stated that the stochastic nature of all the air-ice-ocean wind events studied do not produce perfect examples of class-I or class-II events, but rather these are the general trends observed over many very dynamic episodes.

The divergence and curl involved in class-II wind events is likely due to an atmospheric frontal passage, while the wind relaxation period of class-I events can be associated with larger-scale, less structured wind patterns.

The eOWF response time to the relaxation of wind stress and divergence appears to change depending on the location within MIZ and the details of local gradients in OWF relative to the wind directions. When multiple Cluster 4, class-I wind events are overlapped, the relaxation period pattern can be observed (Figure 34). Similar features of a relaxation period are seen in Cluster 1 (Figure 35). In Class-I wind events, the eOWF response can have a positive or negative reaction to wind stress relaxation.

In class-II events, the sign of eOWF response appears to be dependent on the sign of divergence (Figure 27). In Cluster 4, YD 128 the class-II event has positive wind divergence forcing and a corresponding ice divergence, creating a positive eOWF response. It is observed that in class-II events divergent surface winds force positive eOWF, and convergent winds force negative eOWF, as seen in Figure 27, panel 1 and 5.

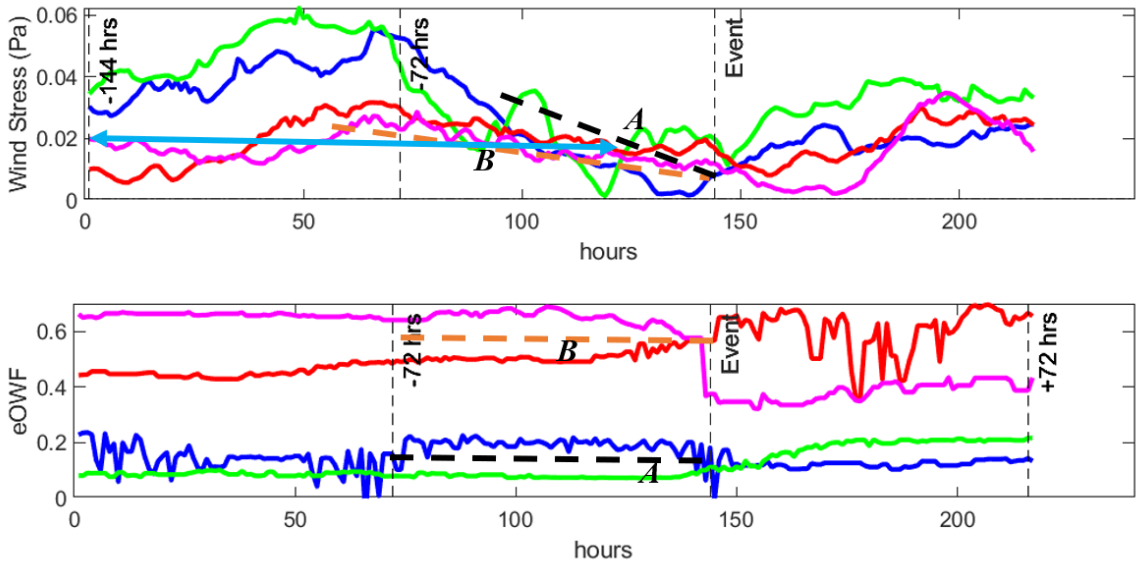

Panel 1 shows wind stress for some class-I wind events in Cluster 4 (YD 114 green, 150 blue, 194 red, 206 magenta). The parallel overlap in the relaxation period is a shared pattern prior to the change in eOWF across class-I events. Panel 2 shows the eOWF response. The corresponding change in eOWF is a repeatable display of the strong relationship between wind stress relaxation and change in eOWF. The light blue arrow points out the minimum threshold of wind stress when ice pack begins to rebalance pressure causing eOWF to change about one day later.

Figure 34. Relaxation period, Cluster 4.

The comparison between the cluster relaxation periods reveals that the ice compression before the wind event may be a factor, which determines the TL of a response in eOWF (Figures 34 and 35). Longer response times (longer TLs) for a corresponding eOWF change may indicate a more compacted MIZ (or thicker ice) prior to the wind event (due to wind stress). A more compacted, less mobile MIZ will need more time for the surrounding ice to relax and re-balance the built-up ice stress, hence an extended relaxation time may be necessary prior to an observed change in eOWF. Additionally, a minimum wind stress threshold exists, under which a relaxation period is most effective in allowing the ice pack to rebalance (Figures 34 and 35). The minimum wind stress threshold may vary for different eOWF levels. This threshold is estimated to be as high as 0.03 Pa for compacted ice (low eOWF), and as low as 0.01 Pa for less stressed ice (high eOWF). The light blue arrow points out the minimum threshold of wind stress when the ice pack begins to rebalance pressure causing eOWF to change (Figures 34 and 35). These thresholds are

chosen because that is the relative values at approximately 24 before eOWF changes. This was seen in all class-I relaxation events.

The more compacted MIZ locations and their associated wind stress are marked by a dashed red line (***A***) producing longer TLs (Figures 34 and 35). The less compacted MIZ locations and their associated wind stress are marked by a dashed black line (***B***) producing shorter TLs.

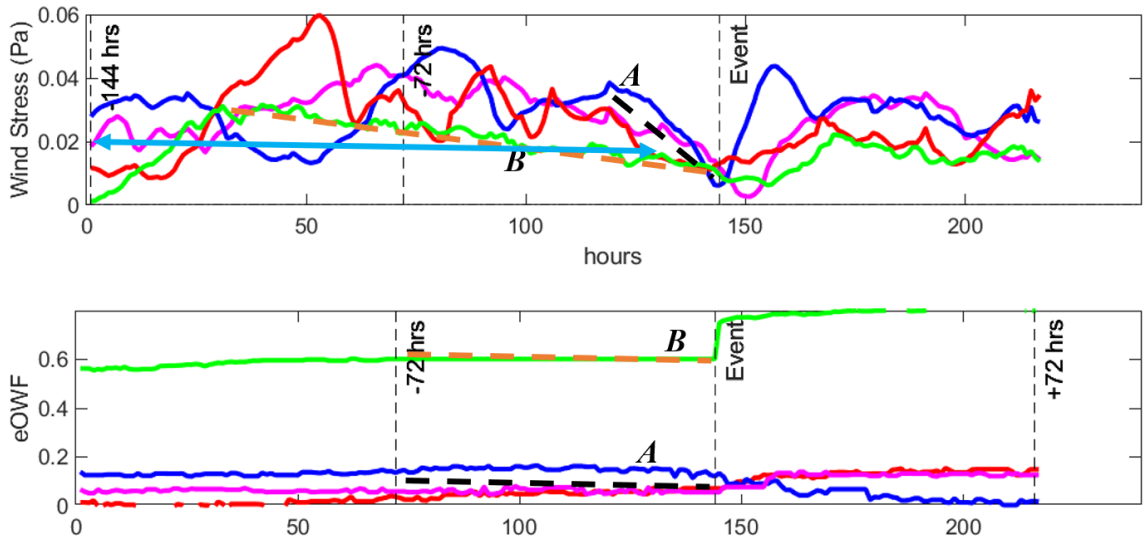

Panel 1 shows wind stress for some class-I wind events in Cluster 1 (YD 119 magenta, 126 blue, 143 red, 195 green). The parallel overlap in the relaxation periods is a shared pattern prior to the change in eOWF across class-I events. Panel 2 shows the eOWF response. The corresponding change in eOWF is a repeatable display of the strong relationship between wind stress relaxation and change in eOWF. The light blue arrow points out the minimum threshold of wind stress when the ice pack begins to rebalance pressure causing eOWF to change about one day later.

Figure 35. Relaxation period, Cluster 1.

To further enhance this concept, the eOWF vs. SSMI OWF plots illustrate that the MIZ at Cluster 4 never fully becomes ice free, and the MIZ at Cluster 1 likely becomes ice free around YD 175 (Figures 36 and 37). This information supports the theory that Cluster 1's physical location probably has less ice pressure in the MIZ during the mid-summer season and therefore needs less time for the eOWF to respond after a wind forcing event. It should be noted that a cross over period around YD 100–120 occurs indicating the eOWF gradient is not continuous through the entire year. Cluster 4 never reaches ice free

conditions in mid-summer causing the MIZ to have some added level of ice pressure, especially when wind stress is present as it is prior to a relaxation period. Therefore, Cluster 4 will need a longer relaxation time (longer TL) during the summer for an eOWF response. This theory proposes that a 2-D surface model with a eOWF gradient is needed to form an accurate response time estimate. This concept allows the possibility for eOWF forecasts when considering the position within the OWF gradient. Generally, highly packed ice will need a longer relaxation period, with very low wind stress, before the MIZ is able to re-balance to a point that a shift in the surface ice (change in eOWF) is sensed among the most compacted ice.

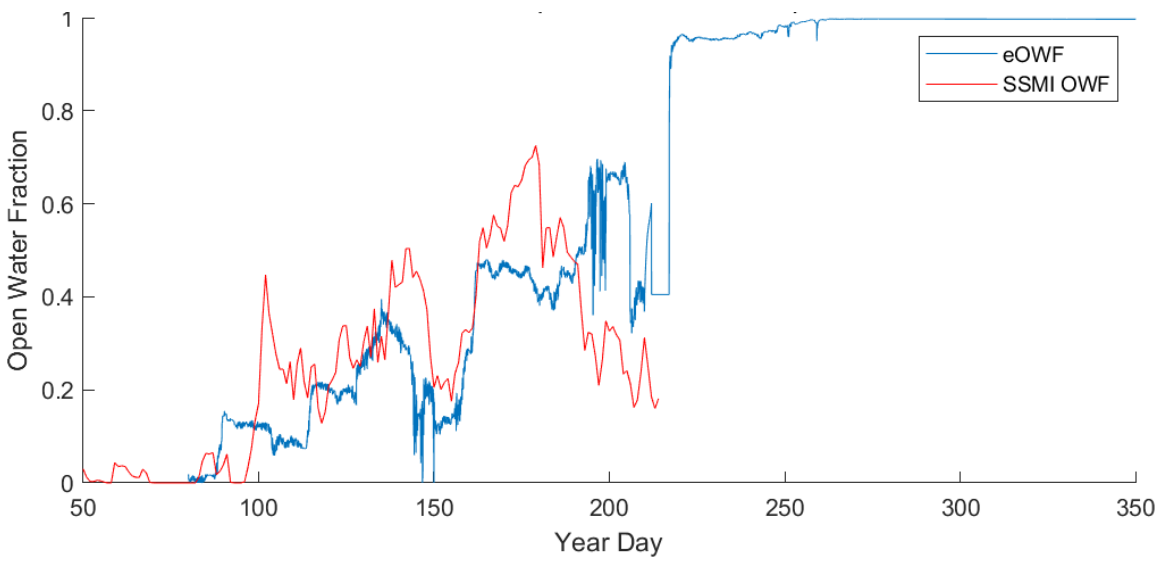

Blue shows eOWF, Red shows SSMI OWF. Cluster 4 reaches an OWF value of about 0.5 by mid-summer. This level of OWF means the MIZ was full of ice for the entire summer causing dampened levels of eOWF change during a wind stress relaxation period due to lower mobility.

Figure 36. eOWF vs. SSMI OWF, Cluster 4.

The sensitivity of the eOWF rate of change d(eOWF)/dt is higher than SSMI OWF rate of change observations (Figures 36 and 37). This sensitivity is due to its direct use of smaller scale eOWF estimates from the in-situ buoy positions within the MIZ, where SSMI is an indirect remotely sensed mean over a larger area. The fact that they both change at the same intervals while being measured in completely different ways attests to the accuracy of each within the complexities of the MIZ. For example, SSMI remote sensing

is not impacted by ocean-ice shearing of buoys positions (obtuse triangle areas), or lateral ice melting, while buoy GPS tracking is not restricted in sensing through thick clouds and fog, and the presence of melt ponds and other surface changes which can distort the radiometer-derived OWF values. Both data sets have strengths and weaknesses but observing their changes in tandem reveal that they confirm each other's data well.

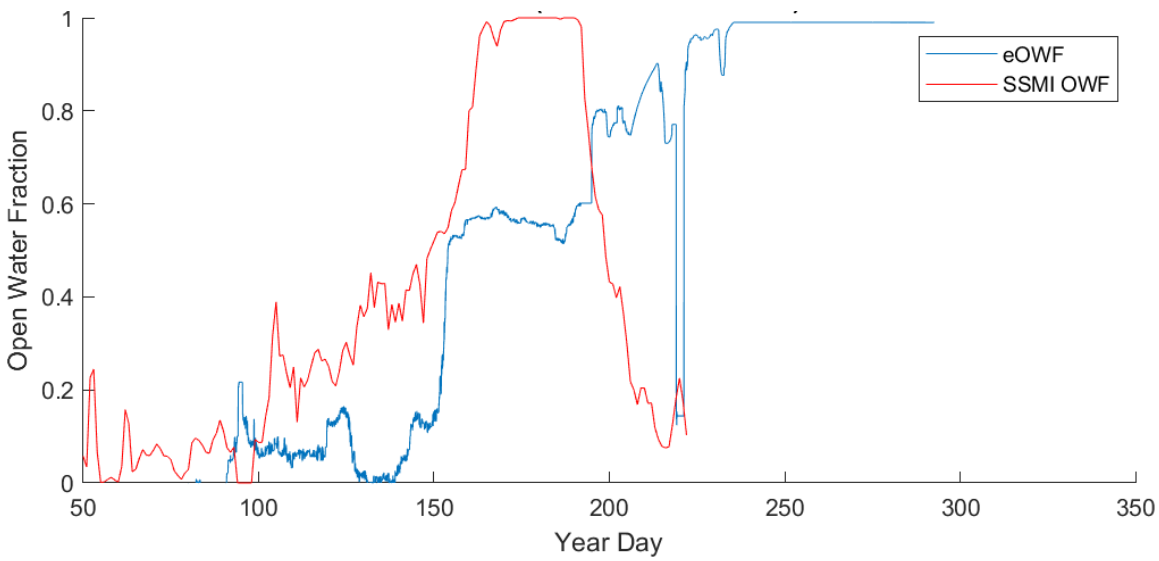

Blue shows eOWF, Red shows SSMI OWF. Cluster 1 reaches an OWF value of 1.0 by mid-summer. This level of OWF means the MIZ was ice free for a month or more. As the MIZ approaches ice free conditions, increased levels of eOWF change occur with wind strrss relaxation due to higher mobility.

Figure 37. eOWF vs. SSMI OWF, Cluster 1.

When we compare the cross-correlation coefficients of each wind event, a pattern arises (Figure 38 and 39). The strong link between eOWF and Wind Stress is confirmed with r-values of 0.91 and 0.89 for Cluster 4 and 1, respectively. The r-values were calculated with a 95% confidence level. The mean r-values for Curl are 0.46 and 0.49. The mean r-values for Divergence are 0.27 and 0.33.

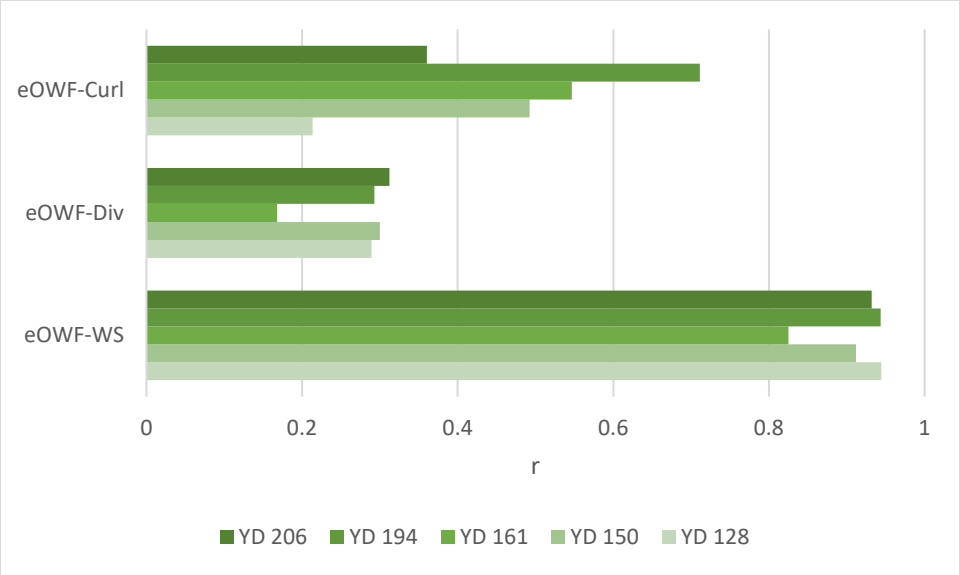

The Cross-correlation coefficients, "r" are calculated with a 95% confidence level. The mean r-value for eOWF and Curl is 0.46. The mean r-value for eOWF and Divergence is 0.27. The mean r-value for eOWF and Wind Stress is 0.91.

Figure 38. Cross correlation coefficient "r," Cluster 4.

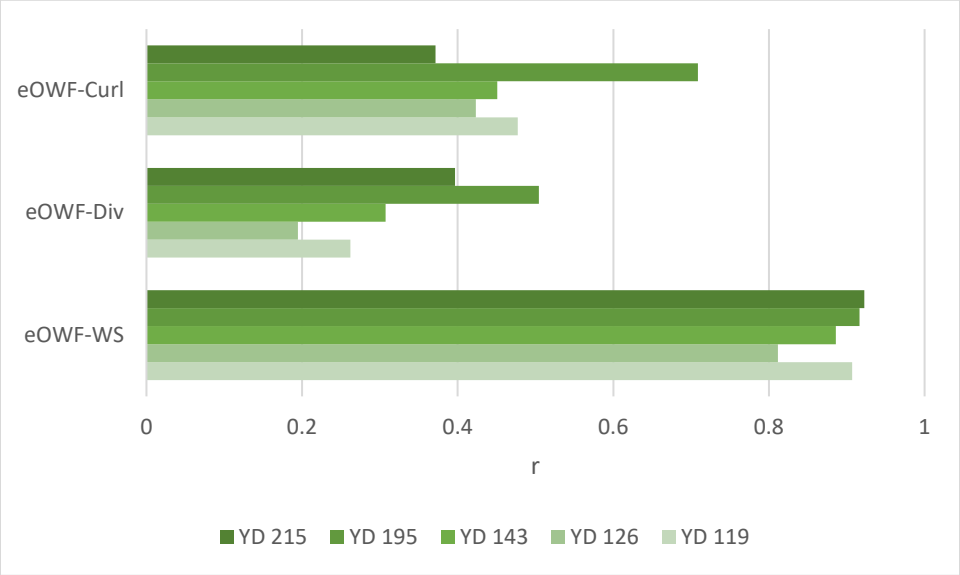

The Cross-correlation coefficients, "r" are calculated with a 95% confidence level. The mean r-values for eOWF and Curl is 0.49. The mean r-values for eOWF and Divergence is 0.33. The mean r-values for eOWF and Wind Stress is 0.89.

Figure 39. Cross correlation coefficient "r," Cluster 1.

When comparing the r-values, curl may appear to be more dominant than divergence as a secondary force. However, this can be misleading as the magnitudes are not dimensionless reflecting the different correlates. By using the NCC, which is normalized for magnitude with the input variances, we can see a less biased result (Figure 40 and 41). The NCC can provide a normalized comparison for each wind event. The NCC can be used to identify the strongest of the competing forcing variables. Additionally, NCC can be used to help classify the wind event as a class-I or class-II. YD 206 is a wind stress event as presented in results (Figure 25 and 26). This is confirmed when we use the NCC for YD 206 (Figure 40). YD 128 was described as a divergence influenced event in results (Figure 27 and 28); however, the NCC leads us to believe there may be more wind stress and curl involved than initially suspected. This is an example of a hybrid event where both wind stress relaxation, and the influence of divergence and curl both play a dynamic role in the evolution of eOWF response.

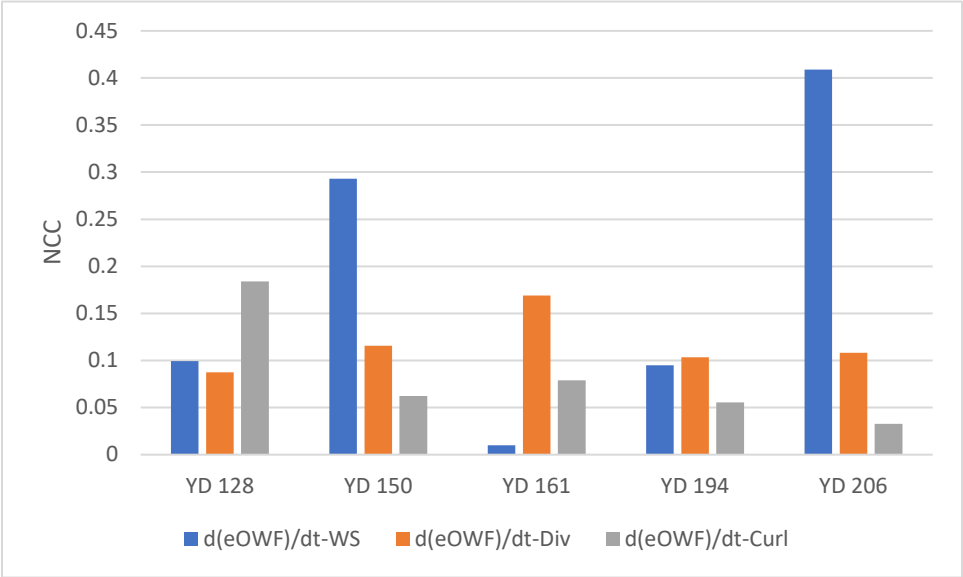

The Normalized correlation coefficients (NCC) are calculated with a 95% confidence level. The NCC assists with determining the dominant forcing within a wind event because it normalizes with respect to magnitude. The mean NCC-values for d(eOWF)/dt and Curl is 0.08. The mean NCC-values for d(eOWF)/dt and Divergence is 0.12. The mean NCC-values for d(eOWF)/dt and Wind Stress is 0.18.

Figure 40. Normalized correlation coefficient (NCC), Cluster 4.

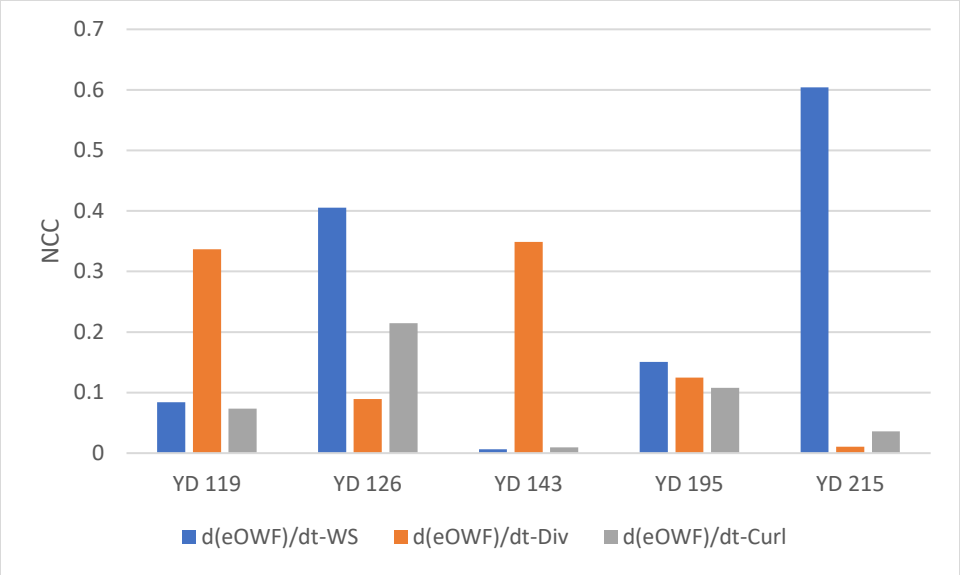

The Normalized correlation coefficients (NCC) are calculated with a 95% confidence level. The NCC assists with determining the dominant forcing within a wind event because it normalizes with respect to magnitude. The mean NCC-values for d(eOWF)/dt and Curl is 0.08. The mean NCC-values for d(eOWF)/dt and Divergence is 0.18. The mean NCC-values for d(eOWF)/dt and Wind Stress is 0.25.

Figure 41. Normalized correlation coefficient (NCC), Cluster 1.

Ice dynamics is complex and may impede the uniform spreading of the ice pack during a relaxation period as a mixture of lead formation, ice subduction and collapse of ice ridges occur. Depending on how much pressure has built up over days or weeks of continuous wind stress, and the state of the ice pack during the summer (initial condition of eOWF prior to relaxation), this will control the amount and rate of OWF response during a relaxation period. In regions of ridging and highly compressed ice, the response may be larger as the piled ice is allowed to sink back into the ocean and spread out over the surface. This interpretation comes from studying all class-I wind events.

If a period of constant moderate wind stress friction keeps the ice softly compacted, but positive divergence is strong in the local wind field, eOWF will slowly increase. Conversely, if strongly negative divergence (convergence) occurs, eOWF will slowly decrease. If a higher magnitude wind stress is applied during a positive divergence period, the increase in eOWF will occur quickly, perhaps due to leads opening, and compressed ice forcing local ridging. This interpretation comes from studying the smaller number of identified class-II wind events.

Curl appears to follow divergent episodes but does not appear independently. Curl is a complimentary force that assists with the compression of ice during negative divergence (convergence) periods and dispersion of ice during positive divergent periods. Because of this rotation, curl and divergence tend to be correlated with each other. At the spatial scale of this research, the measured curl does not appear to ever become a dominant force. However, at larger scales, the curl may begin to have more impact in observations. Curl is a force that likely acts more on the synoptic scale than a local scale, which is the focus of this study. The scale necessary is similar to observing the Beaufort Gyre's mean rotation in response to the Arctic low pressure and the strength of the Artic Oscillation. Atmospheric curl is more likely seen in a response of large swaths of surface ice.

Forcing components (mean wind stress, direction, divergence, and curl) are consistent across both clusters showing that the atmospheric boundary layer and ice interaction dynamics are fairly uniform across the O(100 km) spatial swaths used in this study (Figure 42). The physical locations of Cluster 4 and 1 have different levels of eOWF within the MIZ during mid-summer representing positions within a gradient (Figure 42, panel 5).

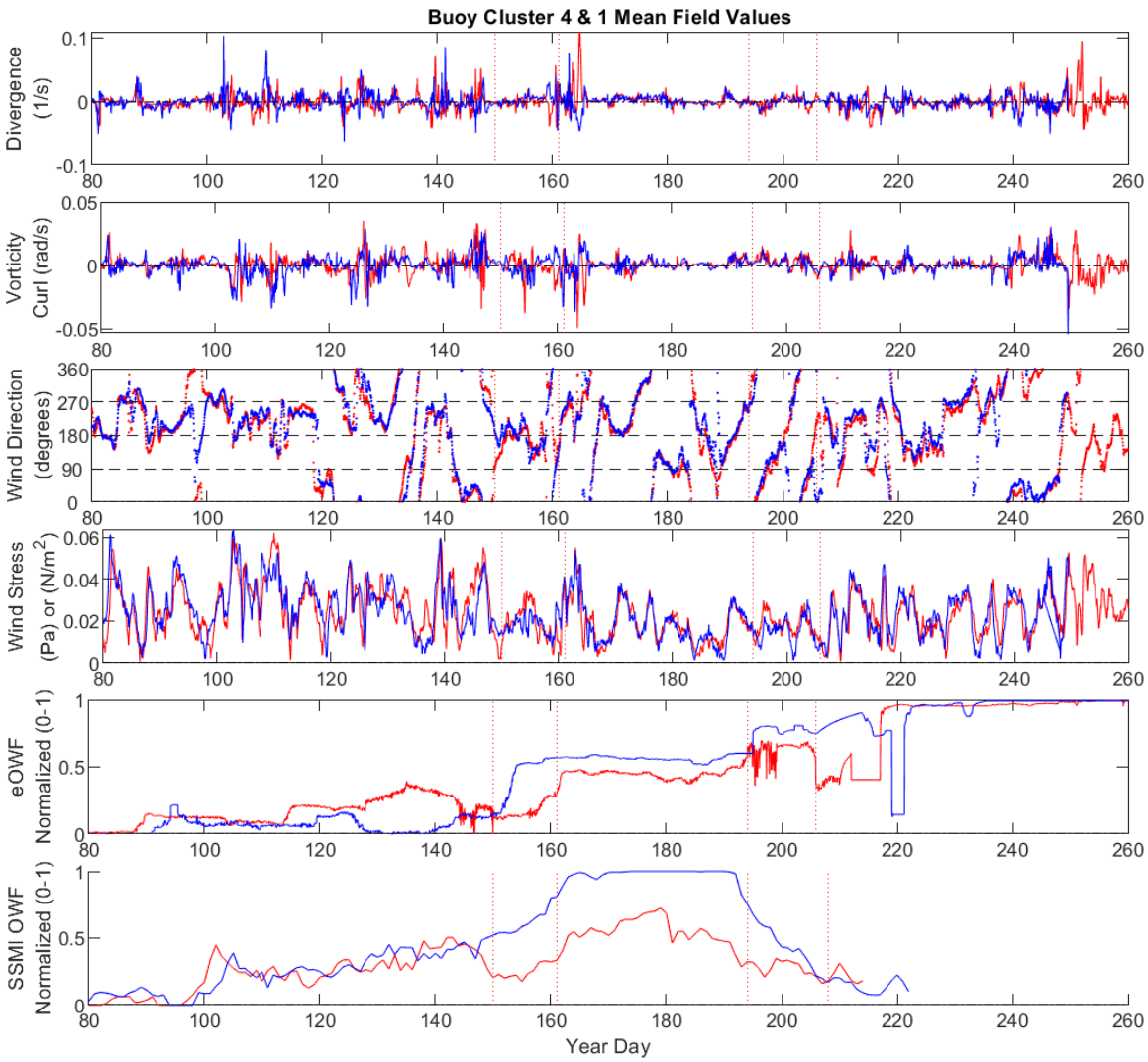

Red is Cluster 4, Blue is Cluster 1. Wind stress forcing (panels 1,2 and 4) and wind direction (panel 3) are consistent across both clusters showing that atmospheric boundary layer dynamics do not change across large spatial swaths. The physical locations of Cluster 4 and 1 are at different levels of OWF within the MIZ during mid summer, as shown in eOWF (panel 5) and SSMI OWF (panel 6). The difference in OWF levels between Cluster 4 and 1, with the same wind stress forcing, illustrates that the location within the MIZ is what determines the increase of eOWF rate of change during each wind event. The gradient of OWF across the MIZ (from highly packed ice to open water) determines the magnitude of response from atmospheric forcing.

Figure 42. Cluster 4 and 1 response comparison.

Observing that the same wind stress forcing across both clusters produces different eOWF responses supports the notion that the local ice pack conditions within the MIZ determines the rate of change of eOWF. For example, the gradient of OWF across the MIZ (from packed ice to open water) on YD 205 determines the magnitude of response from

atmospheric forcing (Figure 43). To produce the same eOWF response, the wind stress relaxation period can be shorter for initial conditions with higher eOWF, than initial conditions with lower eOWF.

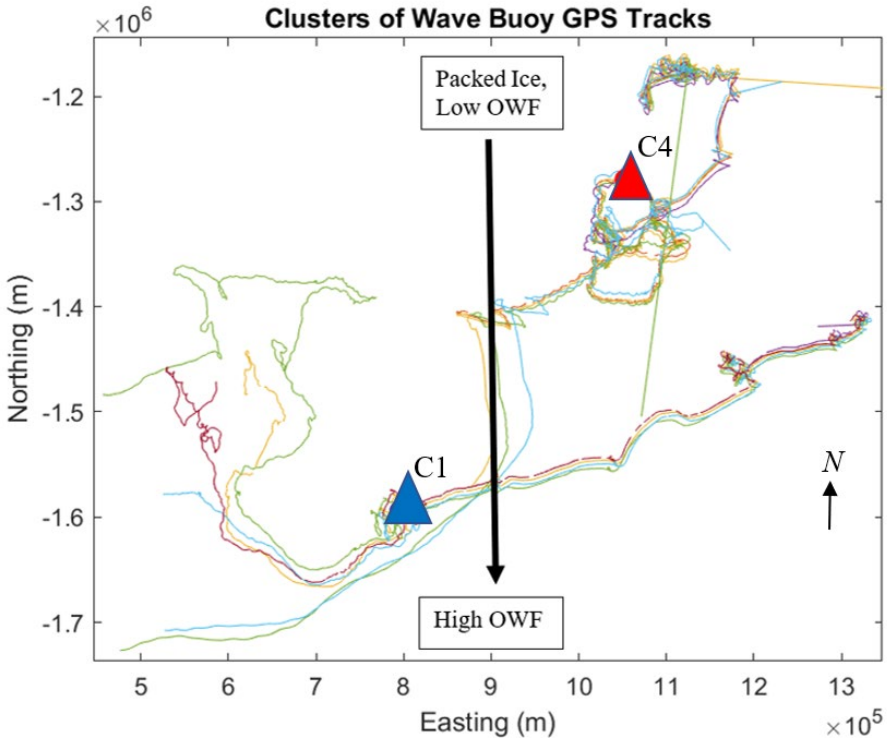

Red triangle is position of Cluster 4 (C4) on YD 205. Blue triangle is position of Cluster 1 (C1) on YD 205. Cluster 4 GPS track is north of Cluster 1 during the peak summer months. The eOWF and SSMI OWF local values for Cluster 4 is less than Cluster 1 at the peak of the summer months (Figure 42, panel 5 and 6). A black arrow depicts the direction of a 2D eOWF gradient across the MIZ from low OWF in the north to high eOWF in the south. The effect of this eOWF gradient prevents the northern Cluster 4 eOWF from reacting in less than a day during a wind stress relaxation period. The southern Cluster 1 eOWF reacts faster than Cluster 4 because of the high OWF gradient, which needs less time to rebalance ice surface pressure during a relaxation period.

Figure 43. Cluster 4 and 1 track comparison, YD 205.

E. CONCLUSION

The relationships between eOWF and wind stress, divergence and curl have clear connections as illustrated in the cross-correlation r and NCC. The mean r-values for each form of surface stress are consistent across both cluster locations studied, suggesting confidence in the results found. A strong link between eOWF and wind stress is confirmed

with mean r-values of 0.91 and 0.89 for Cluster 4 and 1, respectively. NCC with d(OWF)/dt provides an unbiased evaluation of the competing forcing variables during a wind stress relaxation period. The mean NCC across both clusters for wind stress, divergence and curl are 0.22, 0.15 and 0.09, respectively. Findings within all class-I events show that wind stress relaxes approximately 20 hours prior to rapid large changes in eOWF. The full-length TL between the maximum wind stress and the point of lowest wind stress when eOWF rate of change was highest, was found to be approximately 60 hours. There is a lower threshold when eOWF will begin to rebalance that is dependent on the initial state of the ice pack prior to the wind stress event. The threshold seen in this study is approximately 0.02 Pa.

A secondary goal studied the relationship between local eOWF and 25km square grid scale SSMI OWF at multiple sites over the spring to fall of 2014. These timeseries showed similar patterns and changed the same time intervals. Their confirmation of each other, even though they use distinctly different methods of measurement, strengthens confidence in both data sets.

This study found two types of wind events that occur in the MIZ. Class-I has a strong wind stress period followed by greatly reduced wind stress characterized as relaxation events. For class-I events, the relaxation of wind stress predicts a coming sharp change in eOWF, while class-II wind events produce slowly changing eOWF forced by strong local divergence levels. Class-I wind events occurred about four times as much as the class-II evens during the observed period. These classifications are not always distinct, with some events becoming hybrids of both class-I and class-II.

This study has shown the role of a class-I wind relaxation event in allowing eOWF to change by releasing built up ice stress over time. The fact that change in wind direction is not as influential as the cessation of wind stress opposed intuition, but it can often be seen as a secondary factor in OWF change as seen in Figure 30, panel 3. The strong causal signal of eOWF change stems from a pattern repeated across both classes of wind events. Specifically, when there is low wind stress for about 24 hours after a consistently high wind stress, then a corresponding change in eOWF is observed. Therefore, a conclusion from this finding is the fact that change in eOWF (and potentially lead formation) has a very high confidence of incidence following a relaxation in wind stress.

Within the MIZ there are 2-D OWF changes that result in lateral ice pressure gradients that are forced by wind stress (Figure 44). The current OWF pressure gradient at any point within the MIZ is determined by a combination the of the recent wind stress history, and the position within the ice pack lateral gradients of OWF, from highly packed ice to open water. Careful inspection of time sequences of SSMI ice concentration images exhibiting down concentration gradient movement of the ice, suggest that Fick's second law of diffusion is at work within the MIZ. This is further confirmed by the OWF-dependent reaction times of the changes in eOWF after a wind stress relaxation period. The rate of change of eOWF is proportional to location within the 2D total-OWF gradient of the MIZ (Figure 34 and 35).

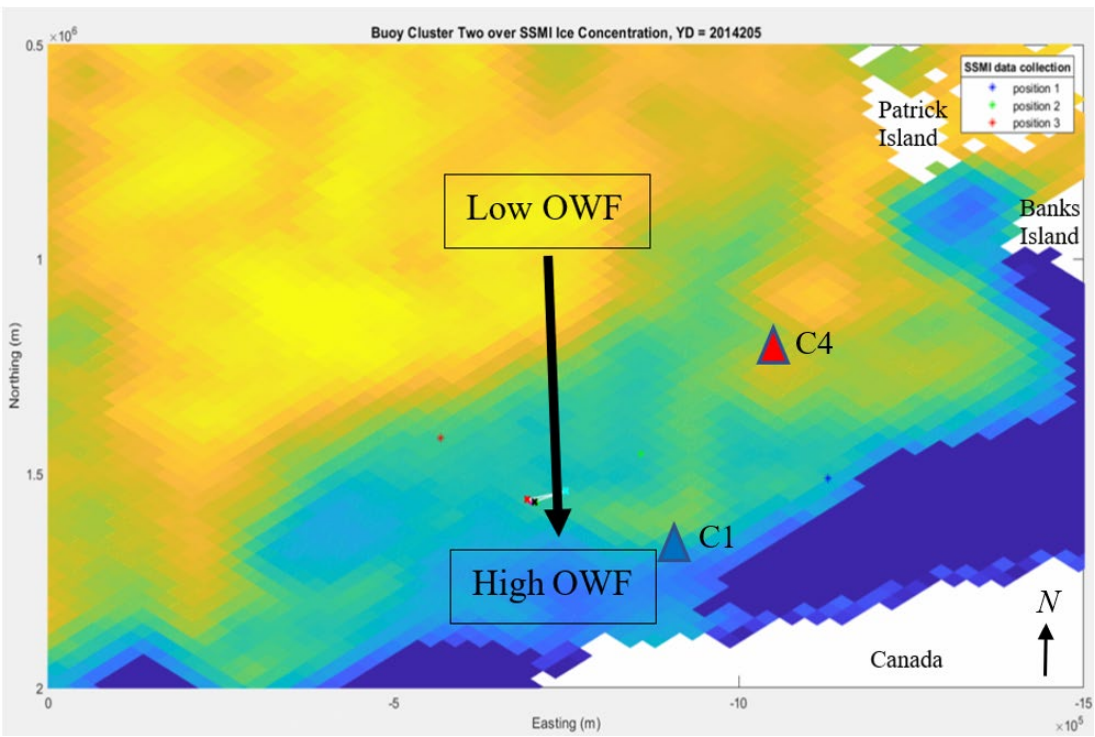

SSMI OWF surface gradient is presented on YD 205 to illustrate the 2D MIZ. Red triangle (C4) is position of Cluster 4 on YD 205. Blue triangle (C1) is position of Cluster 1 on YD 205. OWF changes with cluster position over time. The OWF is determined by position of a cluster prior to a wind event (initial condition). The gradient of OWF across the MIZ will determine the reaction time of eOWF after a relaxation period of low wind stress. If a cluster experiences a relaxation period while in high OWF gradient, the reaction time will be fast (< 24 hours) to cause a change in eOWF. If a cluster experiences a relaxation period while in low OWF gradient of the MIZ, the reaction time will be slow (> 24 hours) to cause a change in eOWF.

Figure 44. SSMI OWF gradient.

There is room for further study in this topic. An investigation of correlation between wind stress magnitude and wind direction in relation to the 2D shape of highly packed ice may show insight into how the competing forces interact dynamically. In late summer, OWF has strong impacts on shortwave radiative heating of the ocean, and the strong ice-albedo feedbacks that rapidly melt-out the MIZ ice, so improved understanding of processes controlling OWF should improve predictions of the thermodynamic processes controlling melt out in the Central Arctic. Results from this research should contribute to increasingly sophisticated ice models used in large scale atmosphere-ice-ocean coupled regional models.

A mandate for science and technology to add to the fight in the Arctic was issued within the Navy's Arctic Blueprint "A Blue Arctic" (USN 2021). This research has answered that call. This thesis has extended methods of determining OWF within the MIZ. This study has established statistical links between OWF and wind stress, divergence, and curl. As the Navy sends new platforms north of the arctic circle to operate regularly, Arctic procedures near the MIZ will mature. Two ways that this study can incorporate a better understanding of the influences involved in changing OWF within MIZ, is by improving MIZ modeling and updating platform routing procedures to include OWF forecasting. Specifically, numerical model simulations of air-ice interaction must have a short coupling timestep O(1-hour) in order to characterize the changes in OWF due to wind events within the MIZ. This will improve ability to hindcast and make future predictions of the MIZ. These examples will improve the Navy's lethality in the Arctic, and lead to more research improvements. Therefore, this research steps towards enabling effective enforcement of a rules-based Arctic region by applying new knowledge. This thesis is a direct contribution towards 'Enhancing Arctic Operations and Building Arctic Awareness,' (DOD 2019).

THIS PAGE INTENTIONALLY LEFT BLANK

SUPPLEMENTAL: ADDITIONAL MATLAB RESULTS

An electronic appendix of all additional MATLAB result figures is included as a supplemental to this thesis. To obtain the supplemental, contact the NPS Dudley Knox Library.

THIS PAGE INTENTIONALLY LEFT BLANK

LIST OF REFERENCES

AMAP, 2007: Arctic monitoring & assessment Program, surface ocean currents, https://www.amap.no/documents/doc/surface-ocean-currents-in-the-arctic/566 (accessed June 21, 2021).

Andersen, S., Tonboe, R., Kern, S., & Schyberg, H., 2006: Improved retrieval of sea ice total concentration from spaceborne passive microwave observations using numerical weather prediction model fields: An intercomparison of nine algorithms. *Remote Sensing of Environment*, **104**(4), 374–392, https://doi.org/10.1016/j.rse.2006.05.013.

AR6, 2021: Sixth assessment report, intergovernmental panel on climate change 2021, The Physical Science Basis, https://www.ipcc.ch/report/ar6/wg1/ (accessed November 5, 2021).

Boulègue, M., 2019: Russia's military posture in the Arctic: Managing hard power in a "low tension" environment. *NATO Defense College*.

Brunke, M. A., Zhou, M., Zeng, X., & Andreas, E. L., 2006: An intercomparison of bulk aerodynamic algorithms used over sea ice with data from the Surface Heat Budget for the Arctic Ocean (SHEBA) experiment. *Journal of Geophysical Research: Oceans*, **111**(C9), C09001–n/a, https://doi.org/10.1029/2005JC002907

Campbell, W. J., Cavalieri, D. J., & Gloersen, P. (1984). Determination of sea ice parameters with the NIMBUS 7 SMMR. *Journal of Geophysical Research: Atmospheres*, **89**(D4), 5355–5369, https://doi.org/10.1029/JD089iD04p05355.

Comiso, J. C., & Kwok, R., 1996: Surface and radiative characteristics of the summer Arctic sea ice cover from multisensory satellite observations. *Journal of Geophysical Research: Oceans*, **101**(C12), 28397–28416, https://doi.org/10.1029/96JC02816.

DOD, 2019: *Department of Defense, 2019-DOD-Arctic-Strategy*.

ECMWF 2014: European Centre for Medium-Range Weather Forecasts, re-analysis-interim data 2014 https://www.ecmwf.int/en/newsletter/147/news/era5-reanalysis-production (accessed November 5, 2021).

Gallaher, S. G., Stanton, T. P., Shaw, W. J., Cole, S. T., Toole, J. M., Wilkinson, J. P., Maksym, T., and Hwang, B., 2016: Evolution of a Canada Basin ice-ocean boundary layer and mixed layer across a developing thermodynamically forced marginal ice zone. *Journal of Geophysical Research: Oceans*, **121**(8), 6223–6250, https://doi.org/10.1002/2016JC011778.

Hibler III, W. H., 1986: *Ice Dynamics, The Geophysics of Sea Ice*. Untersteiner, N., Plenum Press, 577–640.

Higgins, R., Leetmaa, A., & Kousky, V., 2002: Relationships between climate variability and winter temperature extremes in the United States. *Journal of Climate*, **15**(13), 1555–1572, https://doi.org/10.1175/1520-0442(2002)0152.0.CO;2.

Jackson, J. M., S. E. Allen, F. A. McLaughlin, R. A. Woodgate, and E. C. Carmack, 2011: Changes to the near-surface waters in the Canada Basin, Arctic Ocean from 1993–2009: A basin in transition. *Journal of Geophysical Research: Oceans*, **116**, https://doi.org/10.1029/2011JC007069.

Kwok, R., Spreen, G., & Pang, S., 2013: Arctic sea ice circulation and drift speed: Decadal trends and ocean currents: Arctic sea ice motion. *Journal of Geophysical Research: Oceans*, **118**(5), 2408–2425, https://doi.org/10.1002/jgrc.20191.

Kwok, R., 2002: Sea ice concentration estimates from satellite passive microwave radiometry and openings from SAR ice motion: Sea ice concentration and SAR openings. *Geophysical Research Letters*, **29**(9), 25–25–4, https://doi.org/10.1029/2002GL014787.

Lee, & Thomson, J., 2017: An autonomous approach to observing the seasonal ice zone in the Western Arctic. *Oceanography* (Washington, D.C.), **30**(2), 56–68, https://doi.org/10.5670/oceanog.2017.222.

Ivanova, N., Pedersen, L. T., Tonboe, R. T., Kern, S., Heygster, G., Lavergne, T., Sorensen, A., Saldo, R., Dybkjaer, G., Brucker, L., & Shokr, M., 2015: Inter-comparison and evaluation of sea ice algorithms: towards further identification of challenges and optimal approach using passive microwave observations. *The Cryosphere*, **9**(5), 1797–1817, https://doi.org/10.5194/tc-9-1797-2015

Nansen, F., 1902: *The Oceanography of the North Polar Basin*. Green, and Co.

NCAR, 2014: National Center for Atmospheric Research: Special Sensor Microwave/Imager (SS/I), channel F16, https://climatedataguide.ucar.edu/climate-data/sea-ice-concentration-data-nasa-goddard-based-ssmi-and-nasa-team-nt2-algorithm (accessed November 5, 2021).

NPS, 2014: NPS autonomous ocean flux buoy program, wave buoy data, https://www.oc.nps.edu/~stanton/fluxbuoy/links/links.html (accessed November 5, 2021).

NSIDC (National Snow and Ice Data Center), 2021a: Arctic Dynamics, Circulation, https://nsidc.org/cryosphere/seaice/processes/circulation.html (accessed November 5, 2021).

NSIDC (National Snow and Ice Data Center), 2021b: Arctic, marginal ice zone, https://nsidc.org/cryosphere/glossary/term/marginal-ice-zone) (accessed November 5, 2021).

Maslowski, Kinney, J. C., Higgins, M., & Roberts, A., 2012: The future of Arctic sea ice, *Annual Review of Earth and Planetary Sciences*, **40**,625–54, https://doi.org/10.1146/annurev-earth-042711-105345.

MIZ, 2014: Marginal ice zone (MIZ) Project, https://www.apl.washington.edu/project/project.php?id=miz (accessed November 5, 2021).

McPhee M., 1986: *The Upper Ocean, The Geophysics of Sea Ice*, Untersteiner, N., Plenum Press, 370.

Mcphee, M., Martinson, D., 1994: Turbulent mixing under drifting pack ice in the Weddell sea. *Science, American Association for the Advancement of Science*, **263**(5144), 218–221, https://doi.org/10.1126/science.263.5144.218.

McPhee, M., 2008: *Inertial Oscillations in Late Summer*, SHEBA, *Air-Ice-Ocean Interaction Turbulent Ocean Boundary Layer Exchange Processes*. Springer New York, 154–157, https://doi.org/10.1007/978-0-387-78335-2.

Mellor, G. L., 1996: *Introduction to Physical Oceanography.* American Institute of Physics, Woodbury, N.Y.

Mellor M., 1986: *Mechanical Behavior of Sea Ice, The Geophysics of Sea Ice*, Untersteiner, N., Plenum Press, 165–281.

Omstedt, A., Nyberg, L., & Leppäranta, M., 1996: On the ice-ocean response to wind forcing. Tellus. Series A, *Dynamic Meteorology and Oceanography*, **48**(4), 593–606, https://doi.org/10.3402/tellusa.v48i4.12145.

Petty, A. A., Hutchings, J. K., Richter-Menge, J. A., & Tschudi, M. A., 2016, Sea ice circulation around the Beaufort Gyre; the changing role of wind forcing and the sea ice state. *Journal of Geophysical Research: Oceans*, **121**(5), 3278–3296, https://doi.org/10.1002/2015JC010903.

Petty, A. A., Tsamados, M. C., & Kurtz, N. T. (2017). Atmospheric form drag coefficients over Arctic sea ice using remotely sensed ice topography data, spring 2009–2015. *Journal of Geophysical Research. Earth Surface*, **122**(8), 1472–1490, https://doi.org/10.1002/2017JF004209.

Pistone, K., Eisenman, I., & Ramanathan, V., 2014: Observational determination of albedo decrease caused by vanishing Arctic sea ice. *Proceedings of the National Academy of Sciences*, **111**(9), 3322–3326, https://doi.org/10.1073/pnas.1318201111.

Perovich, D. K., 2005: On the aggregate-scale partitioning of solar radiation in Arctic sea ice during the surface heat budget of the Arctic Ocean (SHEBA) field experiment. *Journal of Geophysical Research: Oceans*, **110**(C3), https://doi.org/10.1029/2004JC002512.

Proshutinsky, A., and Coauthors, 2019: Analysis of the Beaufort Gyre freshwater content in 2003–2018. *Journal of Geophysical Research: Oceans*, **124**, 9658–9689, https://doi.org/10.1029/2019JC015281.

Rampal, P., Weiss, J., & Marsan, D., 2009: Positive trend in the mean speed and deformation rate of Arctic sea ice, 1979–2007. *Journal of Geophysical Research: Oceans*, **114**(C5), C05013–n/a, https://doi.org/10.1029/2008JC005066.

Shaw, W.J., T.P. Stanton, M.G. McPhee, J.H. Morison, and D.G. Martinson, 2009: The role of the upper ocean in the surface heat budget of the Arctic Ocean. *Geophysical Research Letters*, **114**, https://doi.org/10.1029/2008JC004991.

Shu, Q., Q. Wang, Z. Song, F. Qiao, J. Zhao, M. Chu, and X. Li, 2020: Assessment of sea ice extent in CMIP6 with comparison to observations and CMIP5. *Geophysical Research Letters*, **47**, https://doi.org/10.1029/2020GL087965.

Spreen, G., Kwok, R., & Menemenlis, D., 2011: Trends in Arctic sea ice drift and role of wind forcing: 1992–2009. *Geophysical Research Letters*, **38**(19), https://doi.org/10.1029/2011GL048970.

Stanton, T. P., Shaw, W. J., and Hutchings, J. K., 2012: Observational study of relationships between incoming radiation, open water fraction, and ocean-to-ice heat flux in the Transpolar Drift: 2002–2010. Journal of Geophysical Research: Oceans, **117**(C7), https://doi.org/10.1029/2011JC007871.

Timmermans, M.-L., J. Toole, and R. Krishfield, 2018: Warming of the interior Arctic Ocean linked to sea ice losses at the basin margins. *Science Advances*, **4**, https://doi.org/10.1126/sciadv.aat6773.

Timmermans, M. L., Proshutinsky, A., Golubeva, E., Jackson, J. M., Krishfield, R., McCall, M., Platov, G., Toole, J., Williams, W., Kikuchi, T., & Nishino, S., 2014: Mechanisms of Pacific summer water variability in the Arctic's central Canada Basin. *Journal of Geophysical Research: Oceans*, **119**(11), 7523–7548, https://doi.org/10.1002/2014JC010273.

Ulaby, F. T., Fawwaz T., Moore, R. K., & Fung, A. K., 1986: *Microwave remote sensing: active and passive*. Addison-Wesley Pub. Co., Advanced Book Program/ World Science Division.

United States Navy, 2021: *Department of the Navy, A Strategic Blueprint for the Arctic*.

USNIC (U.S. National Ice Center), 2021: Ice area coverage, https://usicecenter.gov/Products/ArcticTrendGraph (accessed November 5, 2021).

World Atlas, 2021: Important facts, Beaufort Sea, https://www.worldatlas.com/articles/10-important-facts-related-to-the-beaufort-sea.html/ (accessed November 5, 2021).

THIS PAGE INTENTIONALLY LEFT BLANK

INITIAL DISTRIBUTION LIST

1. Defense Technical Information Center
   Ft. Belvoir, Virginia

2. Dudley Knox Library
   Naval Postgraduate School
   Monterey, California